



## Research Article

# Partially oxidized polyvinyl alcohol + functionalized water soluble multiwalled carbon nanotubes: A new conductive nanocomposite material with promising implications for neuroregeneration

Elena Stocco<sup>a,b,c,d</sup>, Silvia Barbon<sup>a,d,e,\*</sup>, Ludovica Ceroni<sup>f,g</sup>, Marta Confalonieri<sup>a,h</sup>, Giada Pulzato<sup>f</sup>, Samuel Pressi<sup>f,g</sup>, Alice D'Osualdo<sup>a</sup>, Marta Contran<sup>a</sup>, Rafael Boscolo-Berto<sup>a</sup>, Cesare Tiengo<sup>i</sup>, Silvia Todros<sup>d,h</sup>, Piero G. Pavan<sup>d,h</sup>, Veronica Macchi<sup>a,d</sup>, Raffaele De Caro<sup>a,d</sup>, Laura Calvillo<sup>f,g</sup>, Enzo Menna<sup>d,f,g,\*\*</sup>, Andrea Porzionato<sup>a,d,e</sup>

<sup>a</sup> Department of Neurosciences, Section of Human Anatomy, University of Padova, Via Aristide Gabelli, 65 - 35121, Padova, Italy

<sup>b</sup> Department of Women's and Children's Health, University of Padova, Giustiniani, 3 - 35128, Padova, Italy

<sup>c</sup> Department of Surgery, Oncology and Gastroenterology, University of Padova, Via Giustiniani, 2 - 35124, Padova, Italy

<sup>d</sup> Centre for Mechanics of Biological Materials, University of Padova, Via Marzolo, 9 - 35131, Padova, Italy

<sup>e</sup> Foundation for Biology and Regenerative Medicine, Tissue Engineering and Signaling-TES, Onlus, 35030, Padova, Italy

<sup>f</sup> Department of Chemical Sciences, University of Padova, Via Marzolo, 1 - 35131, Padova, Italy

<sup>g</sup> Consorzio Interuniversitario Nazionale per La Scienza e Tecnologia Dei Materiali (INSTM), Via G. Giusti, 9 - 50121, Firenze, Italy

<sup>h</sup> Department of Industrial Engineering University of Padova, Via Gradenigo 6/a - 35131, Padova, Italy

<sup>i</sup> Plastic and Reconstructive Surgery Unit, University of Padova, Via Nicolò Giustiniani, 2 - 35128, Padova, Italy

## ARTICLE INFO

## Keywords:

Multiwalled carbon nanotubes  
Oxidized polyvinyl alcohol  
Nanocomposite hydrogel  
Electroconductivity  
Peripheral nerve regeneration

## ABSTRACT

Carbon nanotubes (CNT) are promising electroconductive nano-scale materials for neuroregeneration. Herein, we report on a new electroconductive composite scaffold made of the polymer 1% oxidized polyvinyl alcohol (OxPVA) combined with functionalized water soluble multiwalled CNT (OxPVA + MWCNT-S) (diazotization reaction). Preliminarily, MWCNT-S were characterized to evaluate the reaction outcome, the degree of functionalization and the dispersibility in water. Thereafter, OxPVA + MWCNT-S nanocomposite membranes were fabricated and analyzed for physicochemical properties (Raman spectroscopy, thermal decomposition, calorimetric properties, electroconductivity), macroscopic appearance and ultrastructure, mechanical behavior, *in vitro* cytotoxicity and *in vivo* biocompatibility. In parallel, OxPVA + MWCNT-S membranes with a linear pattern were also developed and analyzed for interaction with SH-SY5Y cells. Compared to OxPVA, the presence of MWCNT-S (only 0.016 wt%) significantly increased polymer conductivity and imparted a certain porosity without altering mechanical behaviour, as corroborated by uniaxial tensile tests. Neither cytotoxicity nor local signs of inflammation were detected *in vitro* and after subcutaneous implantation (14 and 42 days), proving composite material biocompatibility. OxPVA + MWCNT-S nanocomposite revealed as promising for future electroconductive conduits free from toxic effects amenable to CNT agglomeration within the polymer. Ideally, nerve lesions with wide gaps, may be effectively supported by those "active" devices, overcoming limitations of the available ones. Despite preliminary data, the presence of a linear pattern confirmed to have a beneficial effect over the scaffold/cells interaction.

## 1. Introduction

Recovery of an injured nerve function still represents a significant

medical challenge because of the lack of a safe and adequate supporting environment for nerve regeneration. Currently, autograft placement is the gold standard for peripheral nerve repair in clinical practice;

Peer review under responsibility of Vietnam National University, Hanoi.

\* Corresponding author. Via Aristide Gabelli, 65 - 35121, Padova, Italy.

\*\* Corresponding author. Via Marzolo, 1 - 35131, Padova, Italy.

E-mail addresses: [silvia.barbon@unipd.it](mailto:silvia.barbon@unipd.it) (S. Barbon), [enzo.menna@unipd.it](mailto:enzo.menna@unipd.it) (E. Menna).

<https://doi.org/10.1016/j.jsamd.2024.100762>

Received 13 March 2024; Received in revised form 28 June 2024; Accepted 30 June 2024

Available online 2 July 2024

2468-2179/© 2024 Vietnam National University, Hanoi. Published by Elsevier B.V. This is an open access article under the CC BY-NC-ND license (<http://creativecommons.org/licenses/by-nc-nd/4.0/>).

however, the treatment retains many disadvantages as long surgical procedures, donor site morbidity and possible nerve size mismatch may occur [1]. Considering these limitations, the availability of on-the-bench nerve conduits (NCs) is appealing, being effective in overcoming most of the autografts-associated issues. To date, there are 11 conduits for nerve repair approved by the Food and Drug Administration (FDA). These are made of natural biomaterials (collagen type I [Neuragen, NeuroMatrix, NeuroMend, NeuroFlex, NeuraGen 3D Matrix], extracellular matrix from porcine small intestine submucosa [AxoGuard Nerve Connector], chitosan [Reaxon Plus]) and synthetic biomaterials (polyvinyl alcohol (PVA) [SaluBridge, SaluTunnel], polyglycolic acid (PGA) [NeuroTube], poly (D,L-lactide-co-ε-caprolactone) (PLCL) [Neurolac]). Except for the PVA-based ones (non-biodegradable), all of them display a specific biodegradation profile, ranging from 3 months (NeuroTube) to 48 months (Neuragen) and likely consistent with nerve regeneration time [2,3]. However, commercially available devices used in clinical practice still fail to promote full functional recovery in many patients, especially in case of long gap injuries (>3 cm) [2]: evidences demonstrate that they may be unable to regenerate and recover the complete nerve function, with also performances inferior to that of autografts. It can be assumed that absence of stimuli to guide/stimulate a directed axon and Schwann cell regeneration may contribute to failure in treatment of peripheral nerve long gaps [2,4].

Within this scenario, tissue engineering is currently an attractive field allowing for fabrication of customized NCs, possibly matching the requirements of the ideal device. Following first- and second-generation conduits (based on the not resorbable silicon and biodegradable polymers – polylactic acid, PVA and poly lactic-co-glycolic acid – respectively), experimental evidences support that third-generation nerve guides, along with some basic requirements including biodegradability, biocompatibility, permeability and proper porosity, flexibility, low toxicity and minimal swelling, should also improve neuron regeneration. While “inert” conduits only provide a suitable guidance environment for regeneration, “active” or “smart” conduits are expected to boost nerve regeneration through the release of growth factors, bioactive molecules [5] or exhibiting a certain conductivity [6]. Electrical conductivity is a vital characteristic of smart nerve conduits [7]. Because the nervous system is highly influenced by the electrical stimuli, establishing an electrical environment within conduits may be extremely engaging in terms of morpho-functional outcomes [8]. In fact, electrical stimulation may affect growth and migration of both neurons and support cells as Schwann cells which, through neurotrophic factors secretion, will in turn boost nerve regeneration [9]. Several studies have highlighted that electrical stimulation can accelerate neuronal cells growth from the proximal to the distal stump, thus supporting adequate peripheral nerve regeneration in case of a long gaps [10]. Additionally, electrically conducting scaffolds under electrical stimulation seem to also have a contributory role in stem cells differentiation into neuron-like cells, with a possible great impact in engineered devices development [8].

Since their discovery in 1991, carbon nanotubes (CNT), consisting in hollow cylindrical nanostructures made of rolled graphene sheets in a single wall layer (SWCNT) or in multiwalled layers (MWCNT), elicited right away significant interest in different research fields, appearing as highly desirable especially for biomedical applications [11]. The reason behind that can be traced back to their unique physicochemical properties that together with nanoscale morphology, tunable surface chemistry and exceptional mechanical strength also include electroconductivity, able to assist cell adhesion and growth and differentiation of neurons [12,13]. Specifically, evidences highlight CNTs ability in supporting a sustainable neuronal survival and promoting neuronal outgrowth [14] also boosting neuronal electrical performance [15]. In consideration of this appealing behavior, CNTs stood out as promising materials for neuro-regeneration [16,17]. Moreover, thanks to other peculiar features including a cylindrical morphology and large surface-to-volume ratio, they are recognized as encouraging nanoscale

candidates for incorporation into polymeric networks thus leading to nanocomposite materials [18]. About this, we showed that poly-L-lactic acid nanocomposite scaffolds, based on MWCNT derivatives as fillers, promote neuronal growth and differentiation of human neuroblastoma cells (SH-SY5Y) [19,20] and human circulating multipotent stem cells from peripheral blood [21,22]. Moreover, with human fibroblast cultured on similar scaffolds, we demonstrated how functionalized CNTs can modulate the electrostatic potential at the surface of the composite material, thus tuning cell membrane potential with beneficial effects on their growth [15].

From our previous studies, we deduced that tailored chemical modification of CNTs is a key strategy for their effective and homogeneous dispersion within a polymer phase [23], preventing aggregation and thus enhancing the available surface area and formation of a percolative network [24]. This allows using a smaller amount of nanofiller, that mitigates not only costs, but also possible toxicity issues which may manifest as oxidative stress, inflammatory responses, malignant transformation, DNA damage and mutation, formation of granuloma, and interstitial fibrosis [25]. Specifically, functionalized MWCNTs were obtained through the diazotization reaction based on our previous investigations on different derivatives [20,26]. Although this reaction has already been established, in this case, the procedures were adapted to an aqueous environment in order to achieve good homogeneity of the nanostructure in hydrogel matrices such as PVA. The idea was to introduce benzenesulfonate groups covalently grafted with a good degree of functionalization to achieve optimum solubility in water while maintaining the conductive structure of the CNTs. Moreover, we chose to run the reaction in water under mild conditions, avoiding the use of toxic solvents and strong acids that can lead to residues adsorbed on the material [18,27,28]. Compared to more widely used functionalization approaches such as nanostructure oxidation [29,30], diazotization is a more controlled and versatile method. Oxidation is also known to lead to structural defects that alter the extended  $sp^2$  system and consequently the conductive properties of CNTs. On the other hand, non-covalent methods, such as using surfactants or polymer wrapping [31,32], are less effective and require an excess of solubilizer adsorbed within the material that can be eventually released into the biological environment.

From biopolymers and synthetic polymers to blends, there are numerous materials for nerve conduits fabrication [33]. Within the broad panorama of synthetic materials, partially oxidized polyvinyl alcohol (oxidation degree: 1%) (from here on, OxPVA) emerged as an interesting and versatile option for tissue engineering purposes showing a customizable mechanical behavior, protein-loading/release ability (transforming growth factor beta 1, TGF-β1; ciliary neurotrophic factor, CNTF) as well as biocompatibility and *in vivo* biodegradability [34,35]. OxPVA hollow conduits and wraps, both guaranteed interesting outcomes in animal models of disease (Sprague Dawley sciatic nerve transection) [36–38].

In consideration of previous studies confirming the potential of both OxPVA-derived devices and CNTs in supporting peripheral nerve regeneration (as described above), Here, for the first time, we report on a new electroconductive composite scaffold made of OxPVA + functionalized water soluble MWCNTs (OxPVA + MWCNT-S), while looking for a new material with an appealing profile for future use in fabrication of nerve conduits. Most conductive nerve conduits are lacking in flexibility or permeability; thus the purpose of the work is to evaluate OxPVA + MWCNT-S composite as a candidate for appealing device fabrication, to be used in case of peripheral nerve injury. Considering porosity, softness, and conductance, conductive hydrogels are interesting biomaterials for effective nerve conduits development [39]. Moreover, OxPVA + MWCNT-S-derived conductive conduits, whether electrically stimulated at adequate intensity/frequency/timing, may aid in the process of neurite extension, also increasing secretion of neurotrophic factors from Schwann cells and supporting stem cells differentiation into neuron-like cells with favorable outcomes especially in long gaps

treatment [8].

A thorough characterization was performed both on CNT derivatives to assess effective functionalization and retainment of the desired CNT properties, and on the composite material to confirm and evaluate the possible use as a biomedical device. MWCNT-S reaction outcome and degree of functionalization were evaluated through thermogravimetric analysis, Raman and XPS spectroscopies, in addition, dispersion in water was assessed by dispersibility measurement, size and zeta potential analysis. Thus, OxPVA + MWCNT-S supports were developed exploring specific physicochemical properties (Raman spectroscopy, thermal decomposition, calorimetric properties, electroconductivity, macroscopic appearance and ultrastructure, mechanical behavior, *in vitro* cytotoxicity and *in vivo* biocompatibility). Geometrical cues play an essential role in neuronal growth [40]; in particular, nerve conduits with inner longitudinal grooved pattern are recognized to improve directional outgrowth of the neurons [41]. In consideration of this, OxPVA + MWCNT-S membranes with a linear pattern were also fabricated to verify eventual surface instructive stimulus over SH-SY5Y cells adhesion and proliferation.

According to study evidence, only 0.016 wt% of MWCNT-S were dispersed within the OxPVA matrix, significantly improving the conductive profile of the polymer; no toxic effect amenable to CNTs was highlighted, suggesting no agglomeration of the functionalized MWCNTs within the polymer after mechanical incorporation. Additionally, despite preliminary data, the presence of a linear pattern confirmed to have a beneficial effect over the scaffold/cells interaction. OxPVA + MWCNT-S composite revealed as an interesting blend for tissue engineering purposes, in particular for neural tissue engineering.

## 2. Experimental

### 2.1. Preparation of OxPVA solution

The OxPVA solution was prepared according to previously published protocol [35]. Briefly, 10 g of PVA powder (Sigma Aldrich, S. Louis, Missouri, USA; molecular weight (Mw) 146 000–186 000 Da, 99+% hydrolyzed) was suspended in 200 mL of deionized water (dH<sub>2</sub>O) and solubilized by heating at 100 °C under stirring for 1 h, until complete dissolution of the polymer. After cooling down the system at 37 °C, the partial oxidation (1%) of the solution was obtained by adding 10 mL of potassium permanganate (KMnO<sub>4</sub>) (≥99.0%; Sigma Aldrich) water solution (15.4 mg mL<sup>-1</sup>) + 952 µL of 70% perchloric acid (HClO<sub>4</sub>) (w/w) (Carlo Erba RPE-ACS, Cornaredo (MI), Italy); this step imparted to the solution a brownish color; the reaction run for 1 h at 37 °C, till complete discoloration. Thereafter, the resulting solution was extensively dialyzed against dH<sub>2</sub>O; to this purpose, a membrane with 8000 Da cut-off was adopted. Then the solution was frozen at -20 °C and lyophilized by a freeze-dry system (FreeZone 2.5 L Benchtop Freeze Dry System; Labconco Corporation, Kansas City, MO, USA). For polymer recovery, 16% (w/w) of lyophilized OxPVA was suspended in dH<sub>2</sub>O and the system was exposed to a temperature of 110 °C for 8 h leading to a clear and viscous solution.

### 2.2. Synthesis of MWCNT-PhSO<sub>3</sub><sup>-</sup> (MWCNT-S)

50 mg of purified MWCNTs (4.16 mmol of C) (ACS Material LLC, OD: <8 nm, SKU# CMP00105) were dispersed into 5.0 mL of milliQ water. 36.1 mg of sulfanilic acid (0.05 eq mol<sup>-1</sup> C) (99%; Sigma Aldrich) were dissolved in 3.0 mL of milliQ water and 208 µL of 1 M sodium hydroxide (≥98%; Sigma Aldrich) solution were added to reach neutral pH. The two solutions were mixed and heated to 80 °C under N<sub>2</sub> flux and magnetic stirring. Then, 58 µL of isopentyl nitrite (0.1 eq mol<sup>-1</sup> C) (96%; Sigma Aldrich) were added. After 4 h the reaction mixture was cooled down to room temperature. The dispersion was filtered on a Millipore PC 0.1 µm membrane and the solid product was washed on the filter with 2 x 100 mL of distilled water and 2 x 100 mL of methanol and then

removed from the filter through sonication in methanol. The filtration/washing procedure was repeated twice. The dispersion was finally dried under N<sub>2</sub> flux affording MWCNTs functionalized with benzenesulfonate groups MWCNT-PhSO<sub>3</sub><sup>-</sup> (MWCNT-S).

MWCNT-S were dispersed in milliQ water (5 mg in 5 mL) through pulsed microtip sonication for 1 min (Misonix S3000 Sonicator) with the following pulse parameters: time on = 3 s, time off = 3 s, power level = 2 (4–6 W), and subsequent centrifugation (Thermo Electron Corporation IEC CL 10 centrifuge) at 4000 rpm for 10 min. The supernatant was recovered and filtered over cotton wool and the obtained dispersion was used for characterization and nanocomposite preparation.

### 2.3. Development of nanocomposite scaffolds in OxPVA + MWCNT-S

The MWCNT-S aqueous dispersion was added dropwise to the OxPVA hydrogel solution heated up to 40–50 °C, to reach 0.1 wt% MWCNT-S respect to OxPVA (0.016 wt% respect to the hydrogel weight), and homogeneously mixed with a stainless steel laboratory spatula. Immediately after, the mixture was poured between two glass slides (12 cm × 9 cm) separated by 2 mm-thick spacers. The crosslinking of the polymer into the molds occurred through a freezing-thawing (FT) treatment. Specifically, 6 FT cycles (-20 °C for 24 h/+4 °C for 24 h) were performed; hence, scaffolds with specific dimensions were cut, according to the analyses' requirements. MWCNTs-free OxPVA scaffolds were also fabricated serving as controls. Hydrogel membranes were maintained at -20 °C until use.

### 2.4. Thermogravimetric analysis

Thermogravimetric measurements were carried out on a TGA Q5000IR (TA instruments, New Castle, USA). The analyses were performed in N<sub>2</sub> atmosphere using a 100 µL Platinum-HT TGA pan, a balance gas flow of 10 mL min<sup>-1</sup> and a sample gas flow of 25 mL min<sup>-1</sup>. The measurement method consisted of an isotherm at 100 °C for 10 min followed by a 10 °C min<sup>-1</sup> ramp to 1000 °C. Thermograms were processed using the software Universal Analysis.

Dispersibility in water was evaluated by drop casting 1 mL of the MWCNT-S dispersion on a calibrated TGA pan, and then running an isotherm at 100 °C until constant weight. The measurement was repeated twice, and the mean value was calculated. TGA measurements of hydrogels were carried out on freeze-dried samples and PVA supplied by Sigma Aldrich.

### 2.5. Dynamic Light Scattering

DLS measurements were carried out on a Zetasizer Nano ZS (Malvern, United Kingdom) setting the material as polystyrene latex (RI = 1.590, Abs = 0.010) and the measurement angle at 173°, backscatter (NIBS default). The analyses were carried out at 25 °C, in water dispersant, using low volume disposable plastic cuvettes with a 1 cm optical path, with an equilibration time of 120 s. The resulting value is an average of 3 measurements of 11 runs each, with run duration set at 10 s.

Zeta Potential measurements were carried out in Auto mode at 25 °C, in NaCl 30 mM dispersant, using a Folded Capillary Zeta Cell (DTS1070), with an equilibration time of 120 s. The theoretical model set for the measurement is the Smoluchowski equation. The resulting value is an average of 3 measurements of 10–100 runs each.

### 2.6. X-ray photoelectron spectroscopy

XPS was performed in a custom-made ultra-high vacuum system working at a base pressure of 10<sup>-10</sup> mbar, equipped with an Omicron EA125 electron analyzer and an Omicron DAR 400 X-ray source with a dual Al-Mg anode. Core-level photoemission spectra (C 1s and S 2p regions) were collected in normal emission at room temperature with a

non-monochromatized Al K $\alpha$  X-ray source (1486.3 eV). Single spectra were acquired using 0.1 eV steps, 0.5 s collection time, and 20 eV pass energy.

## 2.7. Raman spectroscopy

Raman spectra were recorded with an Invia Renishaw Raman microspectrometer (50 $\times$  objective). The measurements were performed on dry samples on pre-cleaned glass micro slides (Corning) by irradiating the samples using the 633 nm line of a He-Ne laser at room temperature with a low laser power for a time of 10 s.

## 2.8. Differential Scanning Calorimetry

DSC measurements were carried out on a DSC Q20 (TA instruments), on freeze-dried samples and PVA supplied by Sigma Aldrich. The analyses were performed in N $_2$  atmosphere using a Tzero Aluminum pan with Tzero Lid, working with a gas flow of 50 mL min $^{-1}$ . The samples were previously treated by heating up to 200 °C at 2 °C min $^{-1}$  to remove the residual water trapped in the polymer matrix. Measurements were performed by heating up to 230 °C for the PVA sample, which begins to degrade consistently at higher temperatures, and to 250 °C for the other two samples at 10 °C min $^{-1}$  rates, then cooling down to 30 °C at the same rate. The DSC analysis was repeated for 11 successive heating and cooling cycles to study the reproducibility of the polymer's thermal behavior.

## 2.9. Ultrastructural characterization by Scanning Electron Microscopy

The composite scaffolds ultrastructure was assessed by SEM. Discoidal scaffolds (diameter: 7 mm, thickness: 2 mm) were obtained using a biopsy punch; hence, a transversal cut was performed by a straight blade while the hydrogel membranes were still frozen to minimize eventual artefactual modification. Samples were fixed with 2.5% glutaraldehyde in 0.2 M phosphate buffer (pH 7.2) for 24 h and then dehydrated through ascending graded ethanol series (Scharlab S.L., Sentmenat, Spain). After critical point drying and gold sputtering, observation occurred using a Scanning Electron Microscope (JSM-6490LA; JEOL, Eching b. München, Germany). MWCNTs-free scaffolds were similarly processed (control group).

## 2.10. Conductivity measurement

The superficial conductivity of the composite hydrogel was derived from measuring the superficial resistivity by a Resistivity Test Fixture (Model 8009; Keithley Instruments, Cleveland, OH, USA). The scaffolds (discs, diameter: 60 mm, thickness: 2 mm) were thawed, dried with paper towel and then placed between the electrodes of the instrument. A voltage of 40 mV was applied to the sample using the voltage source built-in an Electrometer/High Resistance Meter (Model 6517b; Keithley Instruments) and both the current and superficial resistivity were measured (10 measurements/sample).

The surface resistivity ( $\rho$ ) [ $\Omega$ ] of the specimen was calculated according to Equation 1:

$$\rho = 53.4 V/I$$

where  $V$  is the applied voltage from the electrometer and  $I$  is the current reading from the electrometer.

In the data post-processing the conductivity (S) of the material was calculated as the inverse of the resistivity ( $\rho$ ). The same procedure was carried out on a OxPVA and PVA membrane used as control.

## 2.11. Scaffolds mechanical behavior

Uniaxial tensile tests were made on a Bose ElectroForce® Planar

Biaxial Test Bench instrument (TA Instruments), with a load cell of 22 N, on 2 mm-thick rectangular samples with 1:4 width-to-free length ratio (width 5 mm  $\times$  free length 20 mm). Tests were carried out up to 100% strain at a constant strain rate of 0.5% s $^{-1}$ . The samples were hydrated during the test by regularly dropping PBS solution on the sample surface. Multiple test repetitions for each material (six for OxPVA, eleven for OxPVA + MWCNT-S) were performed. Force *versus* elongation data were acquired during the tests. Nominal stress  $\sigma$  was calculated as current force divided by the section area of the sample (initial width  $\times$  thickness), while nominal strain was calculated as the ratio between the imposed elongation and the initial length of the sample. Secant modulus was calculated from the nominal stress vs. strain data of each sample, at a strain level of 20%.

## 2.12. Cytotoxicity extract test

To exclude eventual composite material cytotoxicity, a cytotoxicity extract test was performed as previously described [3,38,42]. SH-SY5Y neuroblastoma cells share certain properties with primary neurons, thus being suitable for *in vitro* studies to mimic their attachment and proliferation [43–45]. OxPVA scaffolds ( $\pm$  MWCNT-S) were preliminarily decontaminated through a 2% antibiotic/antimycotic solution (penicillin/streptomycin; Life Technologies, Paisley, United Kingdom) for 1 h under UV light (30 min/side). Thus, once rinsed in sterile PBS, the supports were placed within each well of a 24-well culture plate (Corning, NY, USA) and incubated into SH-SY5Y cells proliferative medium (DMEM/F-12 [Life Technologies] added with 15% FBS [Fetal Bovine Serum; Sigma-Aldrich], 1% non-essential amino acids [Sigma-Aldrich] and 1% antibiotic solution) for 72 h at 37 °C (extract medium). In parallel, SH-SY5Y cells were seeded in a 24-well culture plate (20 000 cells/well) and cultured in proliferative medium for 24 h to allow adhesion prior to replace it with the extract medium. As positive (cytotoxic) control, cells were incubated in culture medium added with 50% dimethyl sulfoxide (DMSO; Sigma-Aldrich), whereas the negative control was represented by untreated cultures. Both treated and control culture were maintained for 24 h and 72 h at 37 °C, 95% relative humidity and 5% CO $_2$ . The effect of extract medium on cell survival was evaluated by the MTT assay. Briefly, at each end-point, after scaffolds incubation in MTT solution (0.5 mg mL $^{-1}$ , 4 h at 37 °C) (Merck Life Science), formazan precipitates were dissolved in 2-propanol acid (0.04 M HCl in 2-propanol) and a microplate autoreader EL 13 (BIO-TEK Instruments, Winooski, VT, USA) was adopted to measure the solution optical density at 570 nm. The results of cell seeding were expressed as total cell number/scaffold, according to a MTT standard curve, preliminary prepared. To this purpose, 1 000, 5 000, 10 000, 20 000, and 100 000 SH-SY5Y cells/well were seeded in 96-well plates allowing adhesion for 12 h. Thereafter, cell viability was measured by MTT assay, obtaining optical density values to associate to each point of the curve. Plotting the assay optical density values on the standard curve it was possible to determine cell number on seeded scaffolds.

## 2.13. In vivo biocompatibility study

*In vivo* biocompatibility of OxPVA + MWCNT-S scaffolds was assessed positioning decontaminated discoidal scaffolds (diameter: 7 mm, thickness: 2 mm) (for decontamination method see Paragraph 2.12) in a dorsal subcutaneous pouch of Sprague Dawley rats; MWCNT-free OxPVA supports were used as control. Samples retrieval and subsequent characterization analyses occurred after 14 and 42 days from surgery.

Animal surgery and husbandry were performed in accordance with the Italian guidelines on the use of experimental animals (DL n. 16/92 art. 5) and approved by the Ethical Committee of the University of Padua and by the Italian Department of Health (Authorization n. 1076/2020-PR, November 10, 2020).



### 2.13.1. Surgery

Six Sprague Dawley rats/end-point were anaesthetized by a binary gas mixture of isoflurane/oxygen and their dorsum was shaved and sterile-prepared with Betadine® (Bayer, Leverkusen, Germany). Subsequently, an incision of about 10 mm in length was performed creating a subcutaneous pouch through blunt dissection. The polymer disks ( $n = 3$  OxPVA:  $n = 3$  OxPVA + MWCNT-S for each end-point) were carefully positioned into and then anchored to the *latissimus dorsi* muscle using Tycron 4/0 sutures; the skin was sutured by absorbable Novosyn 4/0 stitches. After surgery the animals were allowed to recover in the cage and they were administered antibiotic (Bytril, 10 mg kg<sup>-1</sup>) and anti-inflammatory (Rimadyl, 10 mg kg<sup>-1</sup>) therapy for 5 days after surgery. In the following period, they were housed in a temperature-controlled facility and were given laboratory rodent diet and water *ad libitum*.

Euthanasia occurred at day 14 and 42 by carbon dioxide asphyxiation; after dissection, the implants and surrounding tissues were preliminary observed for gross appearance. Thereafter the specimens were excised and properly fixed for subsequent histopathological and ultrastructural (SEM) analyses.

### 2.13.2. Histological and immunohistochemical characterization of the explants

Formalin fixed samples were dehydrated in a graded series of ethanol (Arco Scientifica S.r.l., Padua, Italy) and paraffin-embedded. Hence, 5  $\mu$ m-thick serial sections were dewaxed, rehydrated and stained with H&E and Azan Mallory stainings, according to routine protocols. In parallel, immunological characterization was performed with anti-F4/80 (polyclonal rabbit anti-mouse anti-F4/80, sc-26643-R; Santa Cruz Biotechnology, CA, USA) diluted in PBS 1:800. Antigen unmasking was performed with 10 mM sodium citrate buffer, pH 6.0, at 90 °C for 10 min. The sections were then incubated for 30 min in blocking serum [0.04% bovine serum albumin (BSA; A2153, Sigma-Aldrich) and 0.5% normal goat serum (X0907, Dako, Glostrup, Denmark)] to eliminate unspecific binding, and then incubated for 1 h at RT with the above primary antibodies. Primary antibody binding was revealed by incubation with anti-rabbit/mouse serum diluted 1:100 in blocking serum for 30 min at RT (Dako® EnVision + TM peroxidase, rabbit/mouse; Dako) and developed in 3,3'-diaminobenzidine for 3 min at RT. Lastly, the sections were counterstained with hematoxylin. As a negative control, sections were incubated without primary antibody.

### 2.13.3. Ultrastructural analysis of the explanted scaffolds

After scaffolds explant their ultrastructure was characterized by SEM. Once retrieved, the samples were processed as described in previous paragraph.

## 2.14. Fabrication and characterization of patterned scaffolds

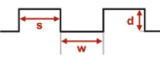
### 2.14.1. Design and development of patterned mold

A mold (120 mm  $\times$  90 mm  $\times$  2 mm (length  $\times$  width  $\times$  height)), characterized by a linear pattern geometry was designed using computer-aided design (CAD) software (Fusion 360, Autodesk, v.2.0.13168, San Rafael, CA, USA). To this purpose, three parameters were considered and modulated including: the groove width (w), the groove depth (d) and the spacing between two grooves (s). The specific parameters used are reported in Table 1.

After modelling, the objects were exported in stereolithography

**Table 1**

Pattern parameters of the mold and of the impressed hydrogel.

	Mold dimensions	Pattern dimensions
		
Groove width (w)	300 $\mu$ m	500 $\mu$ m
Groove depth (d)	500 $\mu$ m	500 $\mu$ m
Spacing (s)	500 $\mu$ m	300 $\mu$ m

format (.stl) into the 3D printer slicer software (Cura software v.4.13.1, Ultimaker, Utrecht, The Netherlands) and converted into a 3D printer format (gcode). Thus, the mold was printed using a commercial fusion filament fabrication (FFF) 3D printer (Ultimaker 2+ Connect, Ultimaker). As for the printing material, PLA polylactic acid) from Ultimaker was adopted.

### 2.14.2. Patterned scaffolds set-up

For patterned scaffolds fabrication the OxPVA solution  $\pm$  MWCNT-S was reconstituted and prepared as previously described. Hence, the solution was poured into the 3D printed mold and a glass slide was placed onto and fasten with a clamp. Six FT cycles occurred for hydrogels crosslinking (see Paragraph 2.3) thus obtaining patterned membranes stored at  $-20$  °C until use.

### 2.14.3. Ultrastructural analysis of the explanted scaffolds

Patterned scaffolds were characterized for their ultrastructure by SEM. The samples were processed as described in Paragraph 2.9.

### 2.14.4. Bioactivity assessment

The bioactive potential of the patterned hydrogel ( $\pm$  MWCNT-S) was evaluated through SH-SY5Y cells seeding. Disc like scaffolds were obtained using a sterile punch (diameter: 7 mm, thickness: 2 mm); once decontaminated (see Paragraph 2.12), the OxPVA patterned scaffolds were placed in a 48-well plate, seeded with 100 000 SH-SY5Y cells/sample ( $2.6 \times 10^5$  cells/cm<sup>2</sup>) and cultured in specific proliferative medium. After 7 days, cell proliferation was assessed with MTT assay; results, expressed as absorbance, were converted to "number of cells grown on the seeded scaffold". Finally the mean value and SD were calculated.

## 2.15. Statistical analysis

Statistical calculations were developed through Prism (v. 9.3.1, GraphPad Software, San Diego, CA, USA). Experimental data were always expressed as mean  $\pm$  standard deviation (SD). Statistical analysis was performed by *t*-Test, assuming unpaired groups and gaussian distribution, in case of two experimental groups, whereas by one-way analysis of variance (Kruskal-Wallis test) and a Tukey multiple comparison test, assuming gaussian distribution, in case of multiple groups. Differences among experimental groups were considered statistically significant with  $p < 0.05$ . Tangent modulus of OxPVA and OxPVA + MWCNTs were analyzed through a non-parametric Mann-Whitney *U* test, considering a significant *p*-value lower than 0.05. All the statistical analyses were carried out by means of Microsoft® Excel®.

To assure data reproducibility, if not otherwise specified, experiments were performed in triplicate and repeated three times.

## 3. Results

### 3.1. MWCNT-S synthesis and characterization

MWCNT-PhSO<sub>3</sub><sup>-</sup> (MWCNT-S) scaffold nanofillers (Fig. 1) were prepared by decorating MWCNTs with benzenesulfonate groups, to provide solubility in water and affinity with the polymer matrix, through covalent functionalization. The synthetic approach, based on our previous modifications [20,26] of the Tour reaction [46], was carried out in water in the presence of sodium sulfanilate and isopentyl nitrite (see Section 2 for details).

The overlay of Raman spectra of pristine MWCNT and MWCNT-S derivatives, showing D (1332 cm<sup>-1</sup>) and G band (1600 cm<sup>-1</sup>) and the D\* overtone (2658 cm<sup>-1</sup>), attested the structural integrity of the carbon nanostructure (Figure A1, Appendix A). The ratio between the intensities of D and G bands (D/G ratio) remained constant after surface functionalization indicating no significant addition of structural defects.

The introduction of sulphur species during the functionalization

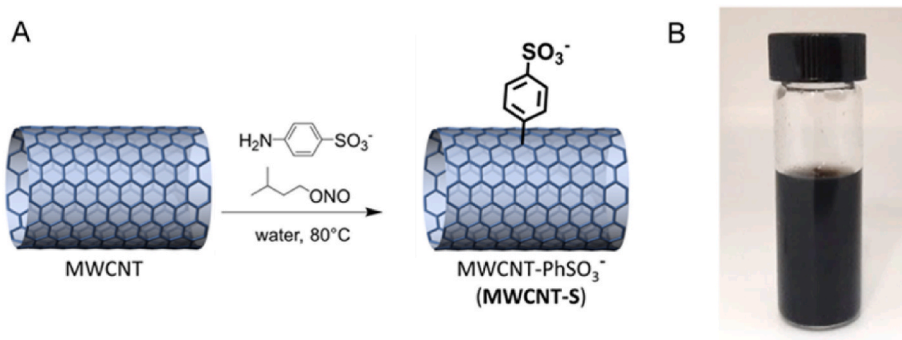


**Fig. 1.** A) Synthesis of MWCNT-PhSO<sub>3</sub><sup>-</sup> (MWCNT-S) scaffold nanofiller through covalent functionalization of MWCNTs; B) water extract of MWCNT-S derivative.

process of MWCNTs was confirmed by X-ray photoelectron spectroscopy (XPS). Fig. 2 shows the S 2p and C 1s XPS regions of the pristine MWCNT and MWCNT-S derivative. The analysis of the S 2p spectrum of the MWCNT-S sample suggested the presence of only one component at 168.0 eV, attributed to the SO<sub>3</sub><sup>-</sup> group, confirming the successful functionalization of the nanostructure with benzenesulfonate groups.

Regarding the C 1s region, the pristine MWCNTs showed a very intense peak at 284.3 eV associated to sp<sup>2</sup> hybridized carbon atoms, characteristic of carbon nanotubes, and a smaller component at 285.3 eV, related to sp<sup>3</sup> hybridized carbon atoms. In addition, the pristine sample showed three additional components at 286.4 eV, 288.0 eV and 289.0 eV, attributed to ternary alcohols, carbonyl and carboxylic groups, respectively. The  $\pi-\pi^*$  transition at binding energy of 290.4 eV was also included in the fit. The MWCNT-S sample showed the same components than the pristine one. A slight increase of the component at 285.3 eV was observed (9.6 at.% vs 8.2 at.% for MWCNT), which can be associated to the presence of C-S interactions, since this component overlaps with the C sp<sup>3</sup> component, confirming the presence of the sulphur functionalities.

Thermogravimetric Analysis (TGA) under nitrogen allowed for thermal behavior of pristine and functionalized CNTs comparison

(Fig. 3). The thermogram of the pristine material showed slight thermal decomposition up to 700 °C denoting high thermal stability in an inert atmosphere. On the other hand, the thermogram of the MWCNT-S derivative showed an additional 5.7% weight loss between 100 and 600 °C with respect to pristine MWCNTs, associated with the decomposition of organic functional groups.

### 3.2. MWCNT-S water dispersion characterization

While pristine MWCNTs are completely insoluble in water, a stable dispersion (see Fig. 1B) was obtained for MWCNT-S with a concentration of  $0.49 \pm 0.01 \text{ mg mL}^{-1}$  (see Paragraph 2.2 for details). The aggregation state of the MWCNT-S dispersion was evaluated through Dynamic Light Scattering (DLS) experiments. Size measurements estimated the mean hydrodynamic diameter of the aggregates of the nanostructure in water. The Z-Average value found was  $163.1 \pm 1.6 \text{ nm}$  and the Pdl of the dispersion resulted 0.381 indicating that the sample was moderately polydisperse. Interestingly, the Zeta potential value resulted  $-44.6 \pm 1.0 \text{ mV}$ , in agreement with the presence of a negatively charged surface.

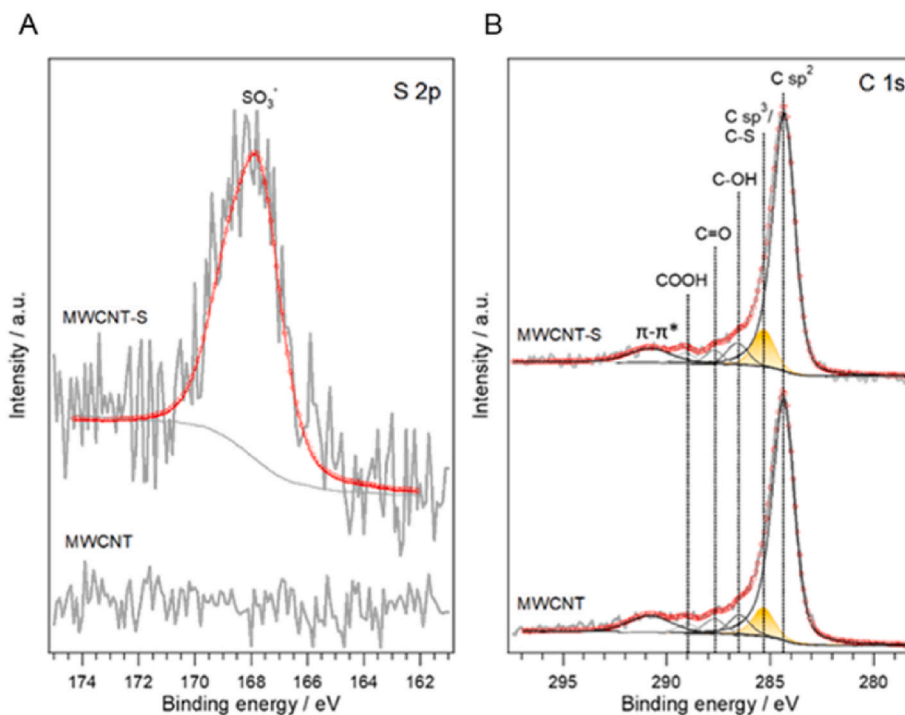


**Fig. 2.** XPS spectra of A) S 2p photoelectron signal in pristine MWCNT and MWCNT-S sample and B) C 1s photoelectron signal in pristine MWCNT and MWCNT-S sample.

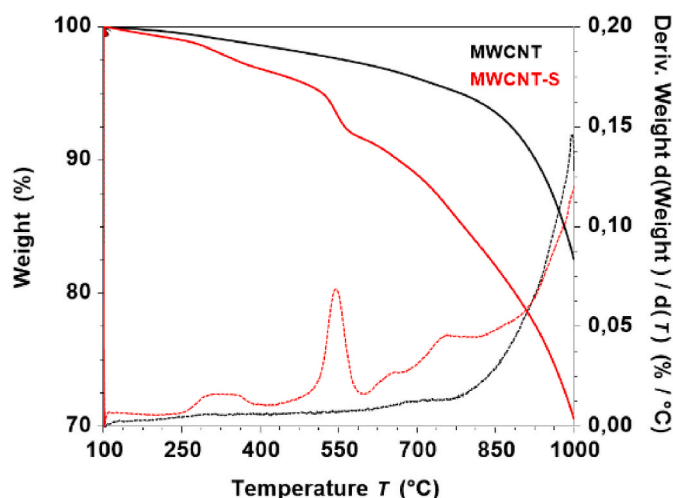


Fig. 3. Overlay of the thermograms (solid line) and the weight loss derivatives (dashed line) of pristine MWCNT and MWCNT-S derivative;  $10\text{ }^{\circ}\text{C min}^{-1}$  heating rate under nitrogen.

### 3.3. Physicochemical properties of the scaffolds (PVA, OxPVA, OxPVA + MWCNT-S)

#### 3.3.1. Scaffolds thermal decomposition

TGA assessed the thermal stability of the polymer matrix before and after the oxidation process and the inclusion of CNTs (Figure A3). Pure polyvinyl alcohol (PVA) showed two main thermal decomposition steps centered at  $243\text{ }^{\circ}\text{C}$  and  $426\text{ }^{\circ}\text{C}$  referable respectively to the elimination of hydroxyl groups and the decomposition of the polyene chain. Instead, in OxPVA the degradation started at higher temperatures showing then similar degradation steps. This indicates a higher thermal stability as a result of the oxidation process. Once incorporated MWCNT-S, another degradation step at  $260\text{ }^{\circ}\text{C}$  appeared, accelerating the thermal degradation process of the material.

#### 3.3.2. Scaffolds calorimetric properties

Differential Scanning Calorimetry (DSC) analysis provided calorimetric characterization of the materials in terms of the glass transition temperature ( $T_g$ ), melting point ( $T_m$ ) and the recrystallization temperature of the polymer ( $T_c$ ) (Figure A4B). A  $T_g$  value of  $90\text{ }^{\circ}\text{C}$  was detected for OxPVA, instead  $78\text{ }^{\circ}\text{C}$  was found for pure PVA, and a further small increase of  $T_g$  was then observed with the addition of MWCNT-S. Concerning the  $T_m$ , a slightly lower value of  $222\text{ }^{\circ}\text{C}$  was found for OxPVA compared to  $226\text{ }^{\circ}\text{C}$  of PVA. Consistently, OxPVA recrystallizes at lower temperatures,  $188\text{ }^{\circ}\text{C}$ , respect to PVA,  $196\text{ }^{\circ}\text{C}$ . The composite OxPVA + MWCNT-S, instead, showed a  $T_c$  at  $191\text{ }^{\circ}\text{C}$  and a  $T_m$  at  $224\text{ }^{\circ}\text{C}$  as if CNT could help the formation of crystalline domains.

The melting enthalpy ( $H_m$ ) and the crystallization enthalpy ( $H_c$ ) were obtained through integration of the melting and crystallization peaks. Heating and cooling cycles were repeated eleven times (Fig. 4a–c), affording a progressive decrease in  $T_m$  and  $T_c$  (Fig. 4d and e), as well as  $H_m$  and  $H_c$  (Fig. 4f and g) for all the three samples. The non-reproducibility of the phenomenon indicates a progressive degradation of the material that can no longer behave in the same way in successive cycles.

The linear fitting of  $H$  and  $T$  values in successive cycles is reported in Fig. 4h and i. The slopes of the graphs represent the speed of the degradation phenomena. A slope value of about 4 was obtained for PVA compared with a value of about 1.5 for OxPVA and OxPVA + MWCNT-S, suggesting a higher tendency to degrade for pure PVA. To validate the hypothesis, the material was weighed before and after the DSC measurements, obtaining a weight loss of 16% for PVA, 5% for OxPVA and 2% for OxPVA + MWCNT-S. A remarkable color change during thermal

cycles was also observed for PVA (from white to orange/reddish), while OxPVA only shifted to a pale-yellow color (Fig. 4a–c).

#### 3.3.3. Scaffolds electrical properties

The electrical properties of the materials were assessed by the measurement of superficial  $\rho$  followed by derivation of hydrogel conductivity. Mean  $\rho$  values of  $1.21 \times 10^9 \pm 1.45 \times 10^8\text{ }\Omega$  and  $5.03 \times 10^9 \pm 2.32 \times 10^8\text{ }\Omega$  were measured for PVA and OxPVA, respectively; thus, the superficial conductivity derived values were calculated as  $8.27 \times 10^{-11} \pm 9.91 \times 10^{-12}\text{ S}$  for PVA and  $2.00 \times 10^{-10} \pm 9.16 \times 10^{-12}\text{ S}$  for OxPVA. In the case of the OxPVA + MWCNT-S composite, however, a  $\rho$  of  $5.53 \times 10^5 \pm 5.74 \times 10^4\text{ }\Omega$  was obtained, corresponding to a conductivity of  $1.81 \times 10^{-6} \pm 2.00 \times 10^{-7}\text{ S}$ . Statistical analysis showed a significant difference between the hydrogels before and after carbon nanotube addition (p-value:  $<0.0001$ ) highlighting the conductive nature of OxPVA + MWCNT-S (Fig. 5).

#### 3.4. Scaffolds macroscopic and ultrastructural appearance

After FT, the cross-linked matrices were easily removable from the glass molds. Macroscopically, the surface of both OxPVA  $\pm$  MWCNT-S scaffolds appeared mainly smooth despite bubbles were observable in presence of MWCNT-S (Fig. 6a and b). Regarding the transversal cross-sections, no cutting defects were detected in both the groups samples (Fig. 6c and d).

Focusing on ultrastructure (Fig. 6e–l), Scanning Electron Microscopy (SEM) analysis showed a rougher surface for OxPVA + MWCNT-S scaffolds than OxPVA scaffolds, at low magnification; whereas, both hydrogels displayed a nano-porous organization, which was finer and more homogeneously distributed in OxPVA + MWCNT-S samples, at higher magnification. The transversal cross-section micrographs highlighted in both hydrogels a structure organized in a preferential direction, even though quite irregular. The presence of a diffuse porosity in OxPVA + MWCNT-S cross-section was evident at both lower and higher magnification.

The images showed good dispersion of CNTs in the hydrogel matrix without visible agglomeration areas.

#### 3.5. Scaffolds mechanical properties

Both OxPVA and OxPVA + MWCNT-S membranes showed a non-linear behavior with stiffening at increasing strain (Fig. 7A). Moreover, no mechanical failure up to 100% strain or permanent strain at maximum applied strain were observed in both materials. The values of secant modulus at 20% of strain of OxPVA and OxPVA + MWCNT-S are reported in Fig. 7B. The statistical analysis did not show any significant difference in the secant moduli at the chosen deformation.

#### 3.6. In vitro evidence of cytotoxicity absence

Cytocompatibility of OxPVA  $\pm$  MWCNT-S scaffolds was evaluated through the cytotoxicity extract test at 24 and 72 h after seeding. According to 3 (4,5-dimethylthiazole-2-yl)-2,5-diphenyltetrazolium-bromide (MTT) assay, no cytotoxic effect was detected over SH-SY5Y cells cultured in extract medium. Percentage of cell viability was higher than the ISO 10993-5:2009 established threshold (set at 70%), at both end-points. Significant differences were only detected *versus* the cytotoxic control (p-value  $<0.0001$ ) (Fig. 8).

#### 3.7. In vivo implant and biocompatibility assessment

The scaffolds were all easy to handle, without giving rise to ruptures while suturing. After the surgical procedures, no rats were euthanized or died before the scheduled end-point due to complications related to surgery. Daily surveillance of the rats in the days after surgery showed neither systemic signs of infection nor local signs of inflammation or

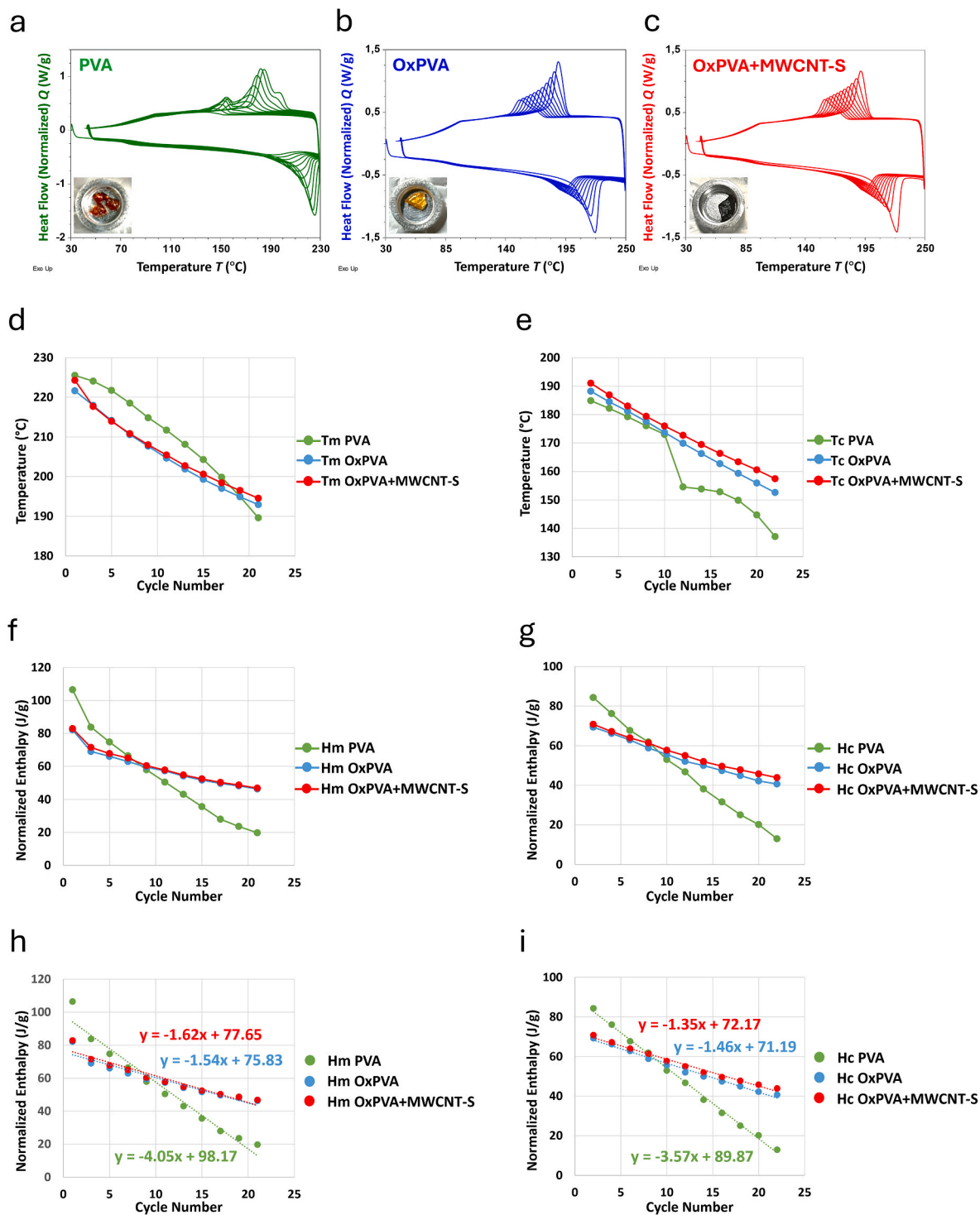


**Fig. 4.** DSC thermograms of PVA (a), OxPVA (b), OxPVA + MWCNT-S (c) in 11 heating and cooling cycles at  $10^\circ\text{C min}^{-1}$ . Pictures of the samples post treatment were reported. Temperature trends of melting (d) and crystallization (e) peak maxima of PVA, OxPVA and OxPVA + MWCNT-S in 22 successive heating and cooling ramps at  $10^\circ\text{C min}^{-1}$ . f) Enthalpy trends of melting (f) and crystallization (g) peak of PVA, OxPVA and OxPVA + MWCNT-S in 22 successive heating and cooling ramps at  $10^\circ\text{C min}^{-1}$ . Linear fitting of melting (h) and crystallization (i) enthalpy values of PVA, OxPVA and OxPVA + MWCNT-S in 22 successive heating and cooling ramps at  $10^\circ\text{C min}^{-1}$ .

rejection.

After 14 days and 42 days of *in vivo* implant, the animals were euthanized and preliminary evidences were gathered at dissection. At both the end-points, in the tissues surrounding the scaffold there was no sign of a significant immune reaction; only a thin fibro-connective capsule, compatible with the type of surgery performed, was detected (Fig. 9a–d). The size and integrity of explanted scaffolds were not

visually compromised (Fig. 9e–h).

The ultrastructure of the excised scaffolds was also analyzed by means of SEM (Fig. 9i–l), to detect eventual modification ascribable to their interaction with the biological environment. Comparing the two end-points, a progressive slight alteration of the scaffolds surface was identified after 42 days of subcutaneous implant; in particular, a certain nanoporosity was more evident for the OxPVA + MWCNT-S group than



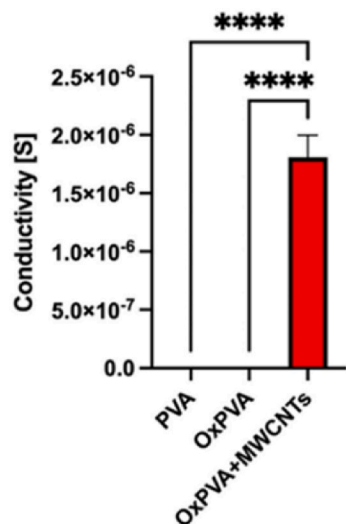


**Fig. 5.** PVA, OxPVA and OxPVA + MWCNT-S conductivity (mean values  $\pm$  SD). A significant difference was detected (\*\*\*\* p-value:  $<0.0001$ ) comparing the three experimental groups.

OxPVA group.

Preliminarily, Hematoxylin and Eosin (H&E) histological analysis considered the overall scaffolds appearance with a focus over the polymer-host interface (specifically, subcutis, upper side; *latissimus dorsi* muscle, lower side) (Fig. 10). OxPVA scaffolds appeared as a thin compact lamina, without ruptures, at both the end-points; the same was for OxPVA + MWCNT-S scaffolds, despite showing one-side peripheral alterations (subcutaneous side, 14 days; muscular side, 42 days) amenable to air bubbles incorporation during MWCNT-S mechanical inclusion.

In accordance with macroscopic evidences and H&E, Azan Mallory staining highlighted the presence of a thin, external fibro-connective tissue surrounding the implants and suggesting the presence of a mild immune reaction compatible with the type of surgery (Fig. 11).

From the immunological characterization, only few F4/80 positive elements, suggesting presence of macrophages, were detected at the subcutaneous and muscular sides, at both the end-points, in the whole cohort (Fig. 12).

### 3.8. Patterned scaffolds development and in vitro behavior

After fabrication by 3D printing, the mold was cleaned to remove excess polymeric material; following FT, the resulting hydrogel was gently stripped out thus showing the specific surface pattern. The overall appearance of the hydrogels was characterized by groove continuity in

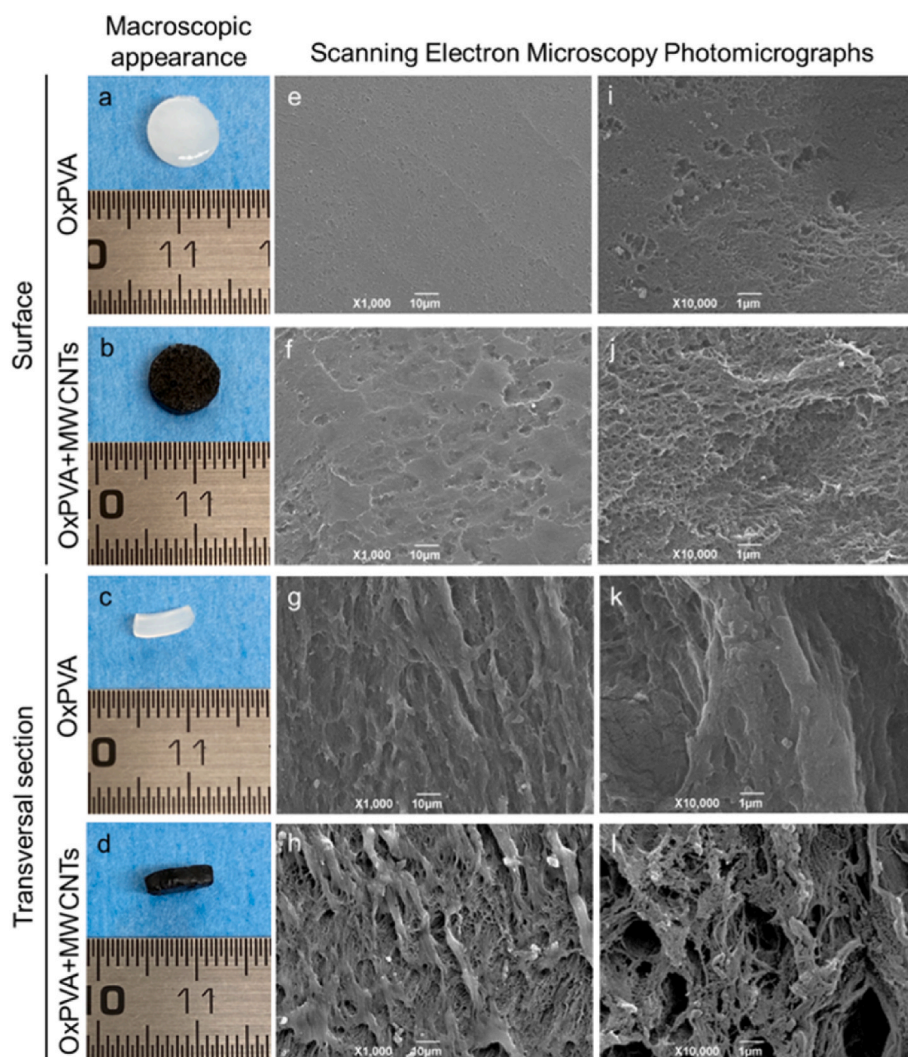


**Fig. 6.** Gross (a–d) and ultrastructural (e–l) appearance of OxPVA and OxPVA + MWCNT-S scaffolds. Surface and transversal sections were both considered.

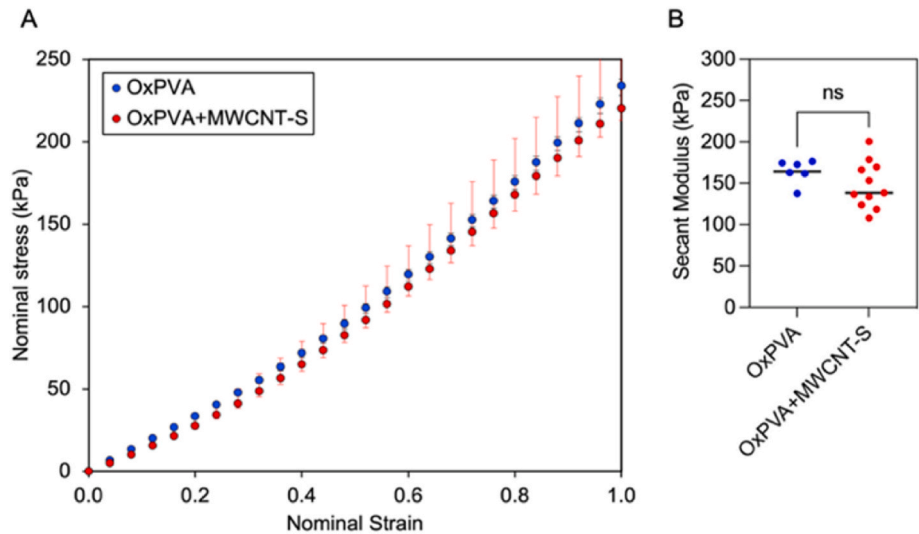


**Fig. 7.** Results of uniaxial tensile tests run on OxPVA and OxPVA + MWCNT-S samples. A) Nominal stress (median and interquartile range) vs. nominal strain; B) secant modulus at 20% strain from tensile tests data. The median (black dash) is indicated. No significant difference is detected comparing the two materials.

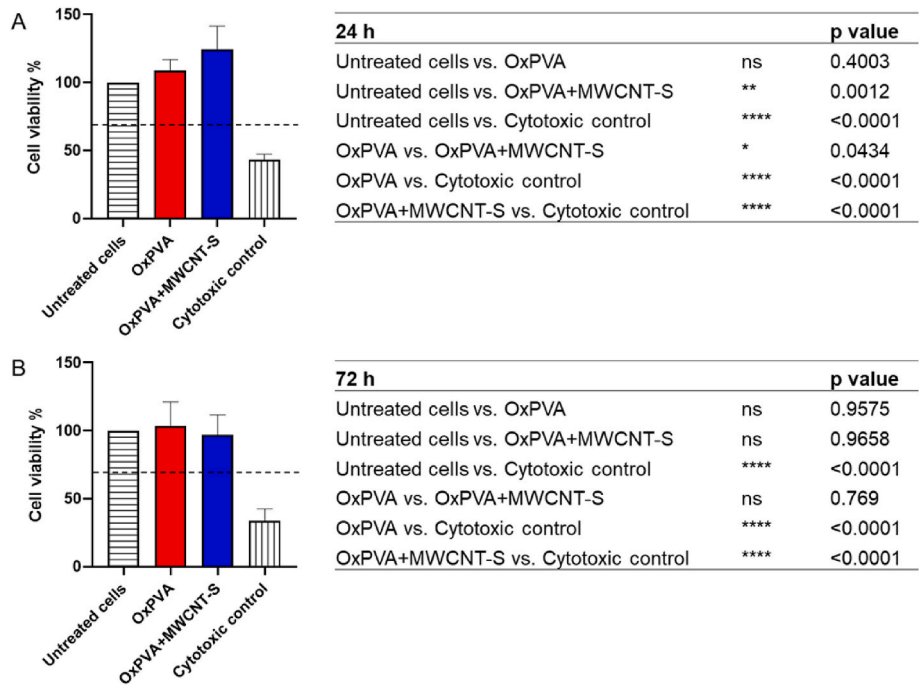


**Fig. 8.** Cytotoxicity extract test. SH-SY5Y cells viability at 24 h (A) and 72 h (B) of culture in conditioned media *versus* negative and cytotoxic controls (\*\*\*\*p-value <0.0001). As for negative control (non-cytotoxic), OxPVA and OxPVA + MWCNT-S cell viability was above 70%, consisting in the threshold set by the ISO 10993-5: 2009 to discriminate non-cytotoxic from cytotoxic materials.

both the experimental groups (Fig. 13). SH-SY5Y cell behavior after seeding on patterned scaffolds was evaluated by MTT assay (Fig. 14). On day 7, only patterned scaffolds in OxPVA ± MWCNTs showed a statistical difference in sustaining cell adhesion/proliferation *versus* smooth seeding surfaces ± MWCNTs (patterned OxPVA *versus* smooth OxPVA, p-value <0.01; patterned OxPVA + MWCNTs *versus* smooth OxPVA + MWCNTs p-value <0.05) (Fig. 14).

4. Discussion

The nervous system is a complex electrical environment; thus, development of engineered devices endowed with electrical

conductivity may facilitate cell-cell communication also boosting cellular signal response [47]. Within this scenario, conductive materials like polyaniline (PANI), polypyrrole (PPy), polythiophene (PTh), and poly (3,4- ethylenedioxythiophene) (PEDOT) have been broadly investigated for nerve conduits fabrication [48]. PANI is inexpensive, easy to obtain and also displays good electrical conductivity; however, it is difficult to manage in experimental studies and undergoes agglomeration [49]. PPy has high conductivity, environmental stability, and low cytotoxicity but due to non-degradability, brittleness, and poor solubility it needs modification to be used in nerve regeneration; several hybrid materials were prepared by combination with biodegradable polymers including polylactic acid, poly (lactide-co-epsilon-caprolactone) and polycaprolactone [50,51]. PTh distinguishes for

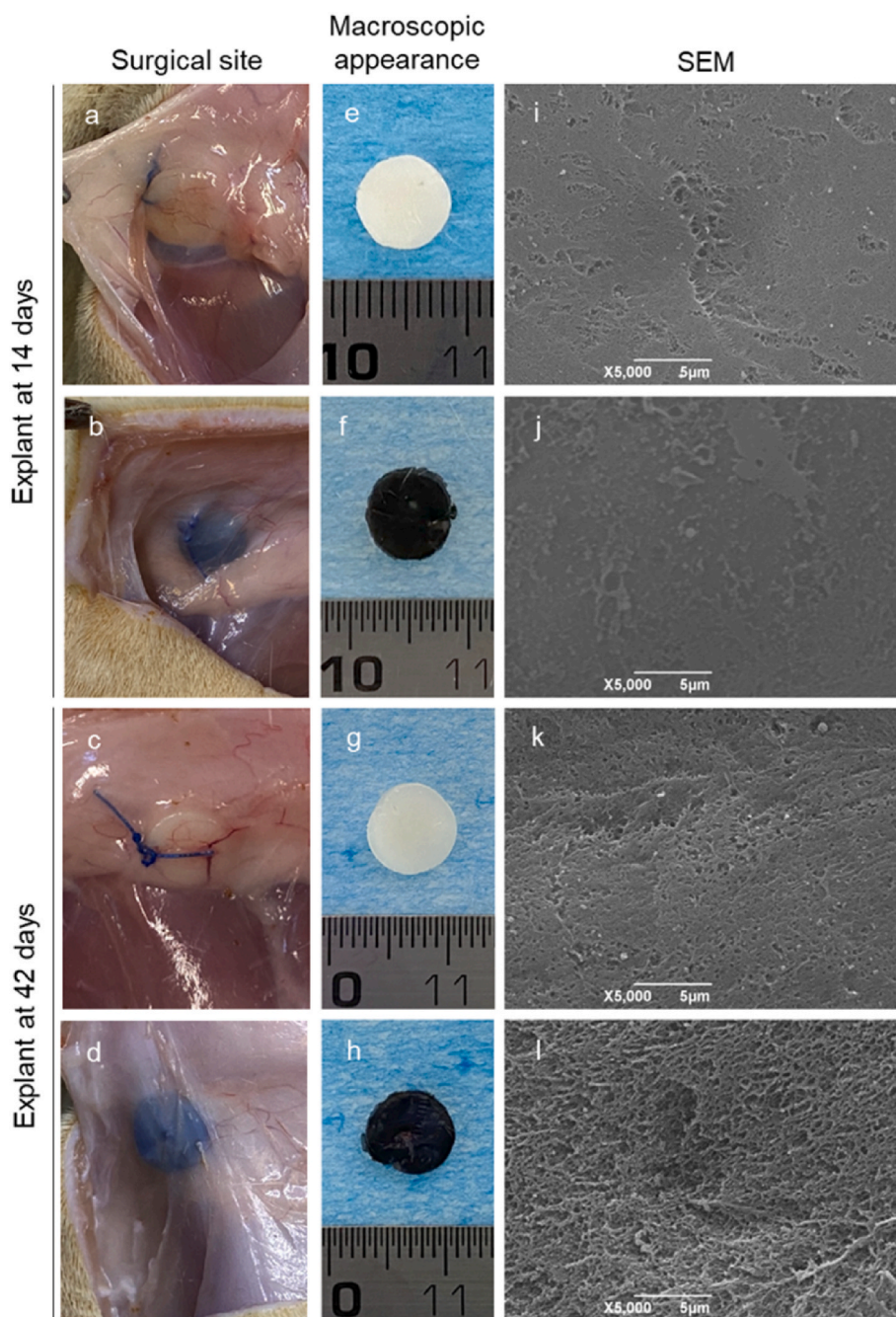


**Fig. 9.** Biocompatibility assessment *in vivo*. Gross appearance and ultrastructural characterization by Scanning Electron Microscopy (SEM) of OxPVA  $\pm$  MWCNT-S scaffolds at the surgical site (a–d) and after excision (e–l) at 14 days and 42 days from surgery. Scale bars: 5  $\mu$ m.

environmental stability and good mechanical strength, but the main weakness is low conductivity. As for PEDOT, it stands out for electrochemical and environmental stability together with stronger electrical conductivity than PTh; however, main PEDOT issues are non-biodegradability and high stiffness [48,52,53].

Together with conductive polymers, also carbon-based materials that include inorganic graphene and CNTs show a high applicability in nerve conduit fabrication [2]. In consideration of that, MWCNT-S were employed here to improve the characteristics of the hydrogel OxPVA (hydrophilicity, viscoelasticity and biocompatibility), obtaining a novel, electroconductive OxPVA + MWCNT-S composite for development of devices to be potentially used in peripheral nerve regeneration. Actually, CNT nanomaterials are one of the widely used organic components embedded into polymeric hydrogels matrix to enhance their intrinsic

properties [54]. However, owing to their poor solubility, to achieve homogeneous dispersion of non-functional CNTs in an aqueous medium would be difficult, thus affecting conductive hydrogels development (anisotropic conductivity) [55,56]. This problem can be solved by modifying the CNTs with different functional groups and, in this study, effective functionalization with benzenesulfonate groups was performed, allowing for preparation of OxPVA nanocomposites with uniformly dispersed MWCNT-S, in the percentage of 0.1 wt% respect to OxPVA. Given the relevance of electrical conductivity for NC applications, we choose a functionalization approach that in the past allowed us to obtain nanofillers for composite materials retaining electronic and electric properties of pristine CNTs, while providing good solubility [24, 57].

Our functionalization is based on the Tour reaction: according to the



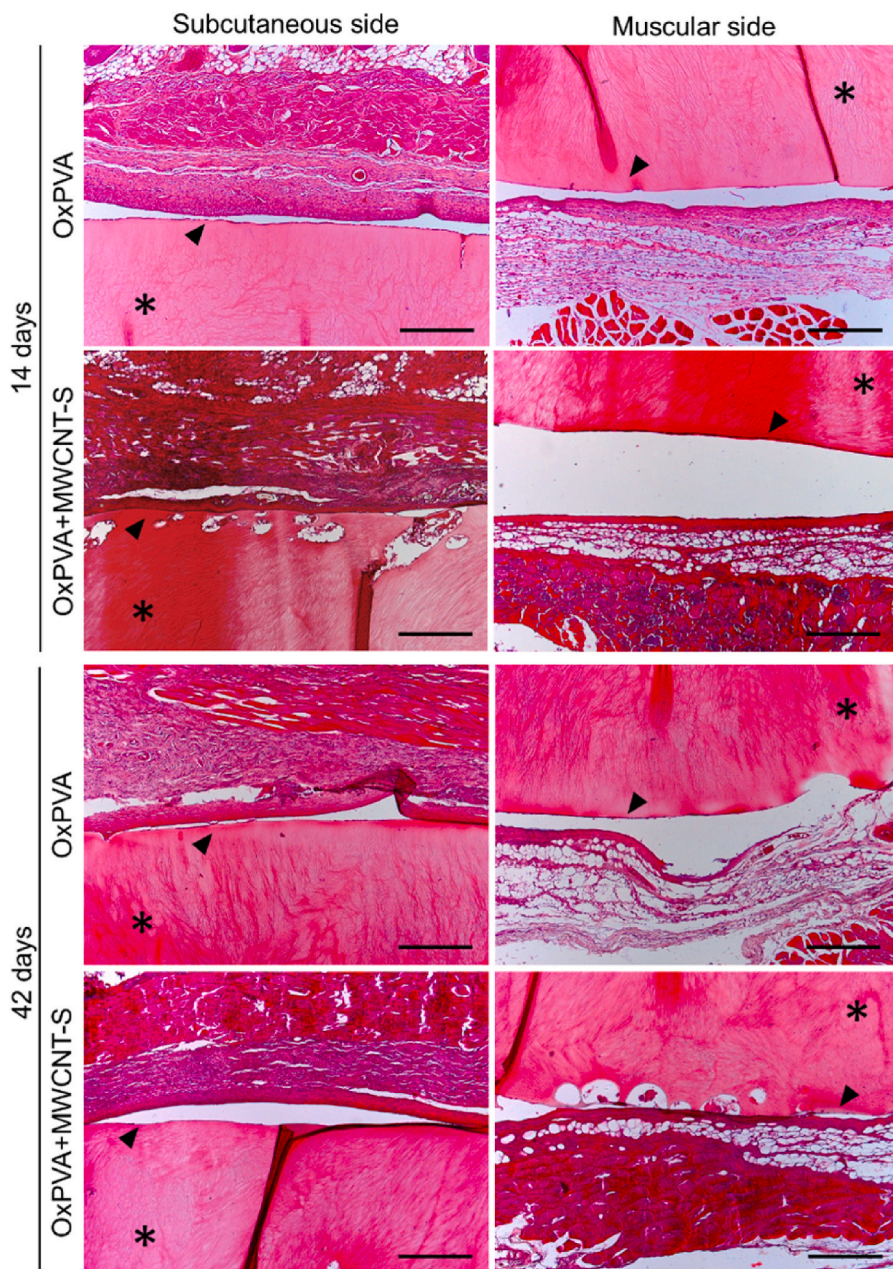


**Fig. 10.** Histological analysis of explants by Hematoxylin and Eosin, at 14 and 42 days from surgery. The interface host tissue/polymer (black arrows) is considered from both the subcutaneous side and the muscular side. The black asterisk shows the OxPVA  $\pm$  MWCNT-S scaffold (Scale bar: 200  $\mu$ m).

literature, a diazonium salt is generated in situ from an aniline treated with isopentyl nitrite, and then reduced to form an aryl radical that reacts with MWCNT basal plane through the Meerwein arylation mechanism [58]. Therefore, before the introduction of the carbon nanostructure into the polymeric matrix, it is first necessarily to assess the structural integrity, the functionalization degree and the dispersibility in water of the MWCNT derivative. Synthesis and characterisation methodologies have indeed been consolidated to confirm our functionalization hypotheses in line with the reproducibility of results supported by our previous publications [24,26].

The Raman spectrum is commonly used to detect the functionalization of the nanostructure by observing the ratio between the intensities of D and G bands (D/G ratio), that increases with the density of defects. In this case, the Raman spectrum of MWCNT-S overlapped with that of MWCNT, showing that the structural integrity of nanotubes is retained, as desired in order to exploit electric conductivity, thus confirming the

proper choice of the functionalization approach.

On the other hand, structural defects introduced by the functionalization are not detected here, as expected considering that only a tiny fraction of carbon atoms in the outer wall are involved, while inner layers are not affected. Moreover, the results could also depend on the wavelength chosen for sample excitation or on the type of carbon nanotubes [59].

Instead, the presence of the functional groups expected from our functionalization strategy was confirmed by XPS analysis. Comparing the literature, the component at 168.0 eV in the S 2p spectrum of MWCNT-S could be attributed to the  $\text{SO}_3^-$  group [60,61]. In addition, in the C 1s region, the component at 285.3 eV increased in the MWCNT-S sample, indicating the presence of C-S interactions. The surface composition of both samples was obtained from the S 2p, C 1s and O 1s peak regions, taking into account the corresponding sensitivity factors. Pristine MWCNTs contained a small amount of oxygen (2.5 at.%). After



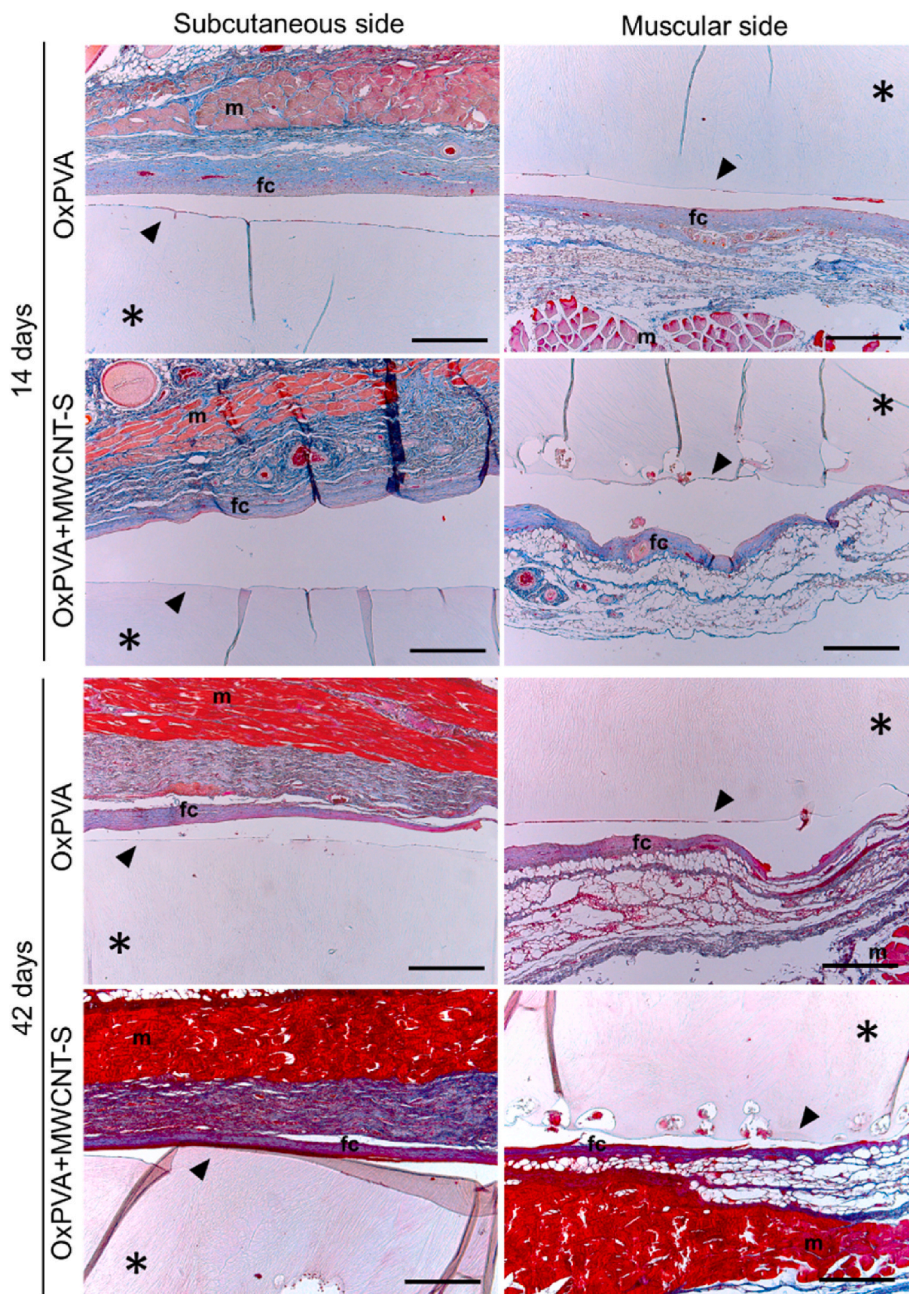


**Fig. 11.** Histological analysis of explants by Azan-Mallory, at 14 and 42 days from surgery. The fibro-connective capsule surrounding the implant is in blue color (fc); the red/dark-red color highlights the muscle fibers (m), corresponding to both the *panniculus carnosus* at the subcutaneous side and the *latissimus dorsi* at the muscular side. The interface host tissue/polymer is highlighted at both the subcutaneous side and the muscular side by the black arrow. The black asterisk shows the OxPVA  $\pm$  MWCNT-S scaffold (Scale bar: 200  $\mu$ m).

the functionalization treatment, 1.0 at.% of sulphur was introduced at the surface, and an increase of the oxygen species was observed (5.5 at. %). As further evidence, the IR spectrum of MWCNT-S reported signals attributable to the presence of the benzenesulfonate groups (see [Appendix A](#)).

A carbon nanostructure functionalized with thermolabile organic groups can be easily characterized by TGA analysis in the  $N_2$  atmosphere. The purpose of the measurement is to recognize the presence of a percentage weight loss attributable to the thermal degradation of the introduced sulphonated groups compared to the pristine material. Specifically, MWCNT-S sample showed a percentage weight loss of 5.7% between 100 and 600  $^{\circ}C$  with respect to MWCNT. Based on this analysis, it is possible to calculate the functionalization degree (FD) as the ratio between the moles of the functional group and the total moles of carbon

[59,62]. The FD obtained for MWCNT-S is 0.44%. It should be noted that this value does not correspond to the spatial density of organic moieties on the MWCNT surface, since the fraction of carbon atoms of the outer wall is unknown. As expected, FD is lower than the percentage of S assessed via XPS, since the latter technique detects only atoms close to the surface, but it further confirms the effectiveness of the functionalization.

Indeed the introduced sulfonate groups demonstrated to be effective in providing solubility properties, as reported in section 3.2, thus enabling homogeneous inclusion of MWCNT-S in OxPVA through mechanical mixing of the corresponding water dispersions, to afford the nanocomposite scaffold OxPVA + MWCNT-S. The high aspect ratio of a single CNT prevents the assumption of a spherical form in water, whereas a carbon nanotube agglomerate can be approximated to have



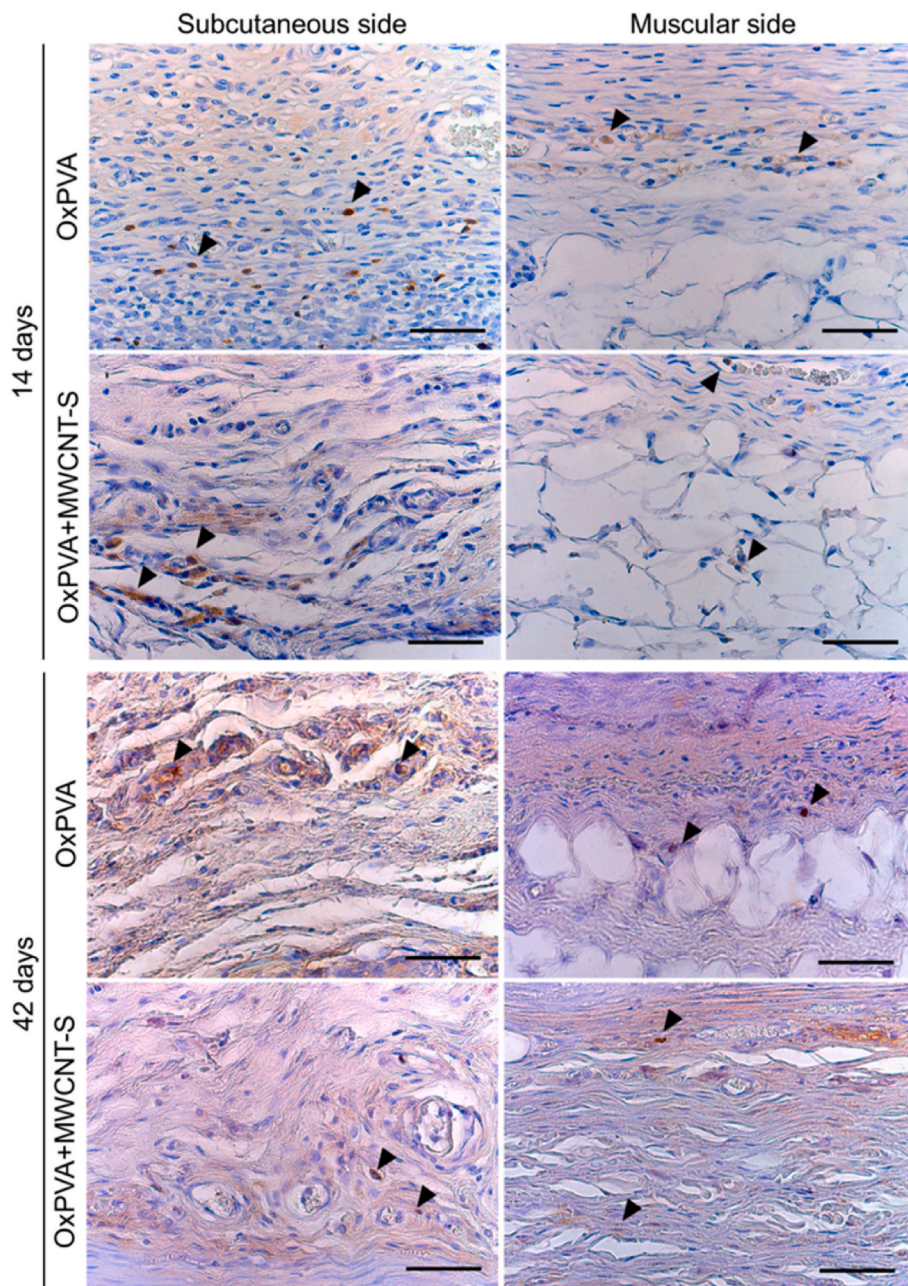


**Fig. 12.** Immunolocalization of F4/80 positive elements, at 14 and 42 days from surgery. The interface host tissue/polymer is considered from both the subcutaneous side and the muscular side. Representative positive elements are showed by the black arrows. (Scale bar: 25  $\mu\text{m}$ ).

an overall spherical shape. Therefore, DLS data cannot be taken as absolute values and Stokes-Einstein equation cannot be applied for the calculation of the radius. However, size measurements still yield an estimate of the mean hydrodynamic diameter of MWCNT-S aggregates in solution [63,64]. In the case of MWCNT-S, a diameter Z-Average value of  $163.1 \pm 1.6$  nm was obtained, which is consistent with other CNT water dispersions reported in the literature [65,66]. The surface charge on the MWCNT-S surface was investigated through Zeta potential measurements. A high negative value of  $-44.6 \pm 1.0$  mV was found, suggesting the presence of a net negative charge on the surface and the formation of a highly stable colloidal dispersion, induced by the introduction of sulphonate groups [67,68], as a further confirmation of the research hypothesis.

Reviewing the literature, it emerges that PVA incorporating carbon nanotubes has been extensively studied in the past years as composite material [69–71] that can be used in the biomedical field [72], including

peripheral nerve regeneration [73]. In previous studies, we already assessed that the oxidation of PVA matrix showed renewed chemical-physical properties that lead to a clear improvement of the material in terms of swelling behavior and biodegradability [35]. In our case, we tested the thermal degradation of the material and the thermal behavior of the crystalline domains by comparing commercial PVA to OxPVA and with the addition of 0.1 wt% MWCNT-S respect to OxPVA weight.

Concerning the TGA of PVA, the literature ascribed the first degradation to the dehydration involving elimination of hydroxyl groups and formation of a polyene structure, while the second weight loss is related to the decomposition of the resulting polyene chain [74–76]. An additional minor degradation step could be detected at 873  $^{\circ}\text{C}$ , probably due to a final decomposition of carbonaceous residues. For OxPVA, the first significant degradation occurs at 363  $^{\circ}\text{C}$ , probably due to the elimination of hydroxyl groups and the evolution of unsaturated aldehydes or

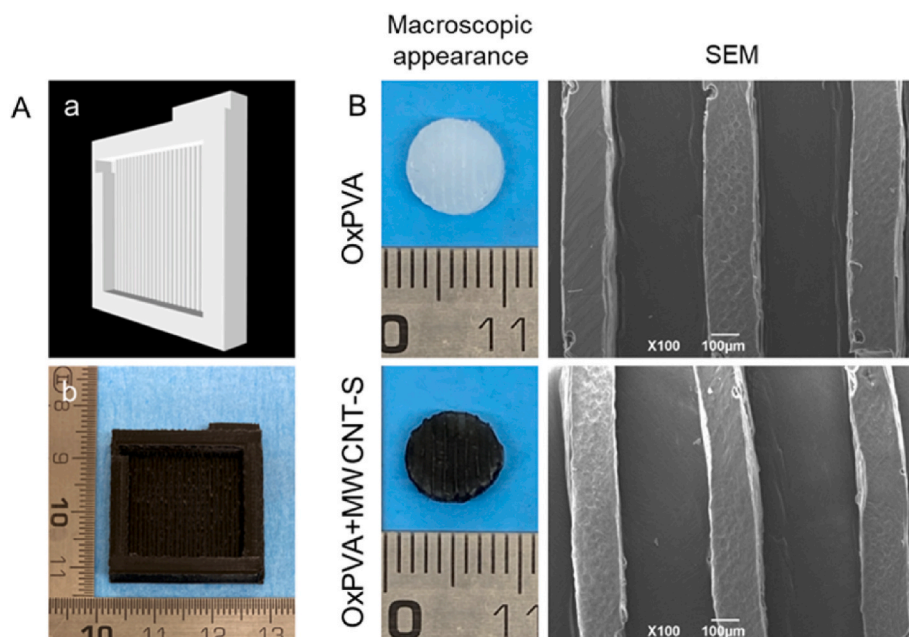


**Fig. 13.** A) Patterned molds design by computer-aided design (CAD) software (a) and fabrication by 3D printer (b). B) Gross appearance and ultrastructure by Scanning Electron Microscopy (SEM) of OxPVA and OxPVA + MWCNTs scaffolds.

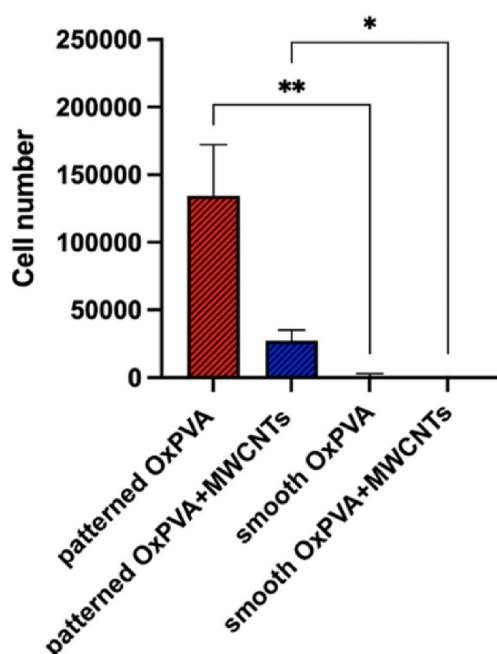


**Fig. 14.** Representation of MTT assay results after 7 days from SH-SY5Y seeding on patterned or smooth OxPVA scaffolds (\* p-value: <0.05; \*\* p-value: <0.01).

ketones [77], at a much higher temperature than the first degradation step for PVA, denoting a higher thermal stability provided by the polymer oxidation process. The next degradation step occurs at the same temperature as for PVA, 426 °C, as expected for the decomposition of a polyene chain resulting from the first degradation. In the case of OxPVA + MWCNT-S, three main degradation stages are observed. The first weight loss at 260 °C is probably due to the presence of carbon nanotubes that accelerate the thermal degradation of the material [78]. The next two weight losses at 337 °C and 422 °C correspond to the main weight losses of OxPVA, slightly shifted to lower temperatures.

PVA is a semicrystalline polymer with chains held together by hydrogen bonds between hydroxyl groups [76]. DSC analysis exhibits several characteristic phenomena of the polymer: the T<sub>g</sub> related to the amorphous part of the material, followed by an endothermic peak corresponding to the T<sub>m</sub> of the crystalline domains and the exothermic peak corresponding to T<sub>c</sub>. Pure PVA showed a T<sub>g</sub> at 78 °C, in good agreement with the literature for high molecular weight PVA [72,79]. The T<sub>g</sub> peak for OxPVA was found at a higher temperature, 90 °C, indicating a lower mobility in the polymer chains, probably due to the replacement of hydroxyl groups with more structurally rigid carbonyl groups. An increase of T<sub>g</sub> of about 0.5 °C was observed upon inclusion of CNTs in the scaffold, in agreement with the T<sub>g</sub> dependence on nanofiller loading reported in the literature and considering the limited (0.016 wt %) CNT content in OxPVA + MWCNT-S [28,78,80]. T<sub>m</sub> and T<sub>c</sub> are also affected by oxidation of the polymer and addition of CNTs. A lowering of T<sub>m</sub> was recorded after oxidation of PVA, from 226 to 222 °C, consistent with the conversion of hydroxyl groups into carbonyl groups, that are no longer able to create hydrogen bonds and cause the melting phenomenon to occur at lower temperatures [35,74]. A slight increase of T<sub>m</sub> was observed upon addition of MWCNT-S: 224 °C for OxPVA + MWCNT-S. This happened during the first heating cycle, as if crystalline domains were stabilized by carbon nanotubes [79]. During the cooling ramp, crystallization occurred at 196 °C for PVA and at 188 °C for OxPVA. The observed T<sub>c</sub> for OxPVA + MWCNT-S is slightly higher (about 3 °C) than for OxPVA, suggesting that MWCNT-S particles could act as nucleation sites aiding the crystallization [78,81]. H<sub>m</sub> and H<sub>c</sub> enthalpies for PVA were higher respect to OxPVA, indicating a loss of crystalline domains due to the oxidation process, in agreement with Raman analysis (see A) [35]. With the addition of CNTs, on the other hand, a slight increase in the heat values is observed, with respect to OxPVA, probably due to a higher crystallinity induced by the fillers as already mentioned [78].

The DSC cycle was repeated eleven times to study the thermal behavior of the material. A progressive decrease in melting and crystallization temperatures and enthalpies was found. A similar behavior was already reported in the literature for PVA, as reported by Thomas and Cebe [82], and attributed to the coexistence of the two thermal phenomena of melting and decomposition, the latter potentially involving changes in macromolecular structure and a decrease in stereo-regularity [83]. As shown by simple linear fittings, the decrease



of Hm and Hc is much faster for pure PVA (slope  $\cong 4$ ) than for OxPVA and OxPVA + MWCNT-S (slope  $\cong 1.5$ ). This observation suggests that the above mentioned tendency of PVA to thermally degrade is mitigated by the oxidation treatment. Finally, especially in the pure PVA sample, more crystallization phenomena coexisting in successive cycles were detected with variation in peak temperature Tc. This was probably due to inhomogeneity of the sample, in terms of chain length and crystallinity [84], while such inhomogeneities seem to be reduced by the oxidation process that brought to the shortening of the polymer chains [35,85].

The electrical conductivity of the material, derived from superficial resistivity measurements, slightly increased after the chemical oxidation process but not enough to change the electrical behavior of the material. Instead, the addition of 0.016 wt% MWCNT-S to OxPVA boosted electrical conductivity of the composite ( $1.81 \times 10^{-6} \pm 2.00 \times 10^{-7}$  S), with an increase of four orders of magnitude compared to pure OxPVA ( $2.00 \times 10^{-10} \pm 9.16 \times 10^{-12}$  S). Other examples in the literature use CNT fillers to increase the electrical properties of a PVA matrix, but they are in general based on the use of surfactants [31] or acid treatments [86]. This requires the use of larger quantities of CNTs to achieve a significant improvement in material properties, thus leading to higher costs and possible toxicity issues. For example, a comparable increase in electrical conductivity is reported in the literature for PVA with a much higher MWCNT loading of 1 wt% [79]. Hence, electrical characterization not only confirms that our functionalization and incorporation strategy provides the desired electrical properties, but also proves that the soluble MWCNT-S derivative can be homogeneously dispersed in OxPVA leading to a percolation network with a very low amount of nanostructure.

Electrical conductivity enables to provide additional electrical stimulation to nerve cells, thus sustaining proper cellular alignment, proliferation, migration, differentiation, signal transduction [9,87]. Interestingly, this ability can favor the restoration of interrupted conduction pathways and maintain the endogenous electrical microenvironment for nerve regeneration [88]. Revising the literature, other studies reported the conductivity values of CNTs-enriched hydrogels. For instance, Mihajlovic et al. [89] measured a conductivity of  $4.7 \times 10^{-3} \text{ S m}^{-1}$  in PE PEG2000, a copolymer composed by polyethylene and poly (ethylene glycol), added with 1.5 wt% MWCNTs versus the CNTs-free counterpart, showing a conductivity of  $2.4 \times 10^{-3} \text{ S m}^{-1}$ ; Salehi et al. [90] measured conductivity values of  $0.34 \text{ S cm}^{-1}$  in a polymer constituted by polylactic acid (PLA), gelatin nanofibrils, 1 wt% of MWCNTs and coated with recombinant human erythropoietin-loaded chitosan nanoparticles, versus  $3 \times 10^{-7} \text{ S cm}^{-1}$  in the non-conductive control. In all the studies reported, the conductivity is higher than that displayed by composite OxPVA. However, two reflections may arise: i) native OxPVA has a much lower conductivity compared to the materials considered by Mihajlovic et al. [89] and Salehi et al. [90]; ii) the MWCNTs concentration in OxPVA is at least one order of magnitude lower compared to that reported in the other studies [89,90].

Attested that oxidation treatment of PVA leads to a material with improved chemical and physical properties, OxPVA and OxPVA + MWCNT-S scaffolds were subsequently characterized for possible *in vivo* applications.

Porosity assessment should be noteworthy for *in vivo* application due to the possibility to exchange and transport nutrients from the extracellular environment into the nerve conduit. Hydrogels are a class of crosslinked polymer chains with varying degrees of porosity. Pore size changes when nanoparticles are introduced in the hydrogel network [91]; thus, because of MWCNT-S addition, the internal microstructure of the OxPVA scaffolds and their surface properties may undergo modification, resulting in different mechanical behavior and biological activities than the MWCNT-S-free counterpart [92]. In transversal section, the composite hydrogels showed an ultrastructure with a certain porosity, differently from OxPVA samples; this evidence may be accordance with Lan et al. [93] and Gubaidullin et al. [94], who highlighted

that CNTs uniform distribution within polyvinyl alcohol/biphasic calcium phosphate mixture and  $\kappa$ -carrageenan-gelatin hydrogel bulk, respectively, led to noticeable influence on sample morphology, in particular on porosity. However, in case of OxPVA, this modification may be also ascribed to the addition of the CNT suspension in aqueous fraction. In particular, the aqueous fraction may have increased the size of the ice-crystals in the freeze-thawing cross-linking process, thus conditioning the polymer chains organization. The CNT mechanical incorporation may have also had contributory role to that, leading to the entrapment of air-bubbles within the polymeric matrix. Differently, considering the external surface, a smoother appearance was detected in both the groups; certainly, using glass slides as mold for membranes fabrication influenced their outer aspect.

The addition of the CNTs could have an impact over the tensile mechanical behavior and the stiffness of the scaffolds, thus affecting the physical properties of the derived devices. In this study the uniaxial tensile tests showed a comparable behavior of OxPVA and the material combined with CNTs. Moreover, a statistical difference was not highlighted in the stiffness of the two materials at the same deformation level that can be found *in vivo* [95]. Although some studies reported an increase in the material stiffness due to CNT inclusion, for this nanocomposite the absence of alterations in the material mechanical properties could be ascribable to the low CNT concentration in the polymer. In fact, a stiffer behavior was observed in materials with a higher CNT concentration [89,96]. Moreover, CNTs are homogeneously dispersed in the PVA matrix, thanks to functionalization: for this reason, no preferred orientation of the CNTs is expected which could result in an anisotropic behavior with a stiffer direction, as observed in the case of vertically-aligned CNTs in an hydrogel matrix [97].

Previous studies already proved the ability of OxPVA conduits to guide nerve regeneration *in vivo*, sustaining the physiological loads without rupturing [36]. In conclusion, according to these results, OxPVA + MWCNT-S based conduits can be considered suitable for nerve regeneration from the mechanical point of view.

Besides mechanical properties, excluding the biomaterial cytotoxicity and proving its biocompatibility is fundamental in the perspective of *in vivo* implant. While biocompatibility of both PVA [98–100] and OxPVA [2,34–38,85,101,102] is well established and supported by *in vitro* and *in vivo* studies, this aspect is of paramount importance whether referring to CNTs. There exists a direct and strong relationship between toxicity and agglomeration state of CNTs; well-suspended CNTs are less toxic to both *in vitro* cell lines and *in vivo* [103]. On this regard, previous studies are relatively scarce, and often contradictory [92], thus a specific and material-targeted evaluation is required. The results of cell experiments *in vitro* showed that the addition of 0.1 wt% in MWCNT-S to OxPVA is safe for SH-SY5Y proliferation at both 24 h and 72 h (as corroborated by statistical analysis). Possibly, these evidences further confirm what stated by Serrano et al. [104], demonstrating that CNT toxicity is greatly reduced whether they are embedded in a hydrogel matrix. Accordingly, various CNT-hydrogel composites have been developed and reported in the literature, including both natural and synthetic polymers (e.g., polyacrylamide, polymethacrylic acid, polyethylene glycol, polysaccharides, gelatin, collagen) [105]. Certainly, together with the agglomeration state and concentration, also CNT diameter and length impact over biocompatibility [106].

To furtherly prove OxPVA + MWCNT-S biocompatibility, the eventual immune reaction, mainly ascribable to *in situ* release of substances, was assessed *in vivo* (three animals/group were used for each end-point to guarantee for results reproducibility). The nano-composite scaffolds did not elicit any severe inflammation in Sprague-Dawley rats, at both 14 days and 42 days from surgery: this attitude is in accordance with previous evidences gathered for OxPVA alone [35]. Moreover, the presence of a thin connective capsule was detected in the two groups without significant differences. The overall results, characterized by no symptoms of acute inflammation, suggest that implants were well tolerated. Certainly, evaluation of outcomes associated with longer



in-vivo permanence of the scaffolds (eventually combined with higher percentages of MWCNT-S) would be beneficial for a deeper knowledge of the composite material; possibly, this may represent a study limitation.

Surface microtopography can confer to biomaterials specific bioactive properties, including growth instructive signals (growth rate and orientation, migration, ECM proteins production) affecting nerve regeneration [38]. In particular, linear patterned grooves proved to enhance an adequate neuron directional growth, avoiding neuroma formation descending from an uncontrolled neurite growth [107–110]. It is well established that smooth OxPVA scaffolds do not promote cell adhesion and proliferation *in vitro* [36]; therefore, a physical stimulus (ultrastructural organization of the groove) was here included to optimize the scaffolds performances and a pilot *in vitro* study occurred to preliminarily verify the effectiveness of this kind of modification. Experimental evidence reported in the literature showed scaffolds' enhanced biological outcomes with groove width dimensions comparable to cells soma size (neural cells size ranging approximately from 5 to 60  $\mu\text{m}$ ) [108]. For instance, Sun et al. [109] impressed PCL films with a groove displaying width and depth of 20  $\mu\text{m}$  and 3  $\mu\text{m}$ , respectively, in turn observing the growth of long and aligned NG108-15 cell neurites (NG108-15 cell size between 16 and 25  $\mu\text{m}$  [111]). In this study the development of OxPVA-based patterned scaffolds was achieved through the fabrication of PLA molds by a FFF 3D printer. Unfortunately, the instrument available revealed a limited dimensional accuracy and precision, conditioned by the nozzle size and the XY resolution; therefore, only a pattern with growth width, growth depth and spacing of 500  $\mu\text{m}$ , 500  $\mu\text{m}$ , and 300  $\mu\text{m}$ , respectively, was obtained, representing a study limitation. Although the pattern dimensions were different from that reported in the literature, an enhanced OxPVA-based scaffolds bioactivity was highlighted, as showed by the SH-SY5Y cells behavior: differently from Schwann cells or PC12 cells forming neurites that assume an elongated orientation, SH-SY5Y cells proliferate better on wider grooves as forming clusters [38]. Despite further studies are required, including the fabrication of more fine grooves as well as the use of different cell populations (PC12, primary Schwann cells), the results clearly highlight that introducing physical cues on OxPVA is a valid method to improve the biomaterial bioactivity.

## 5. Conclusion

The MWCNTs functionalization with benzenesulfonate groups showed to be effective in overcoming the main limit of these materials, consisting of their intrinsic hydrophobic nature that may hinder the fabrication of composite hydrogels, leading to agglomerate formation with consequent toxicity. Compared to other existing methodologies, this specific type of nanostructure functionalization allowed the use of a minimum amount of material within the polymer matrix, ensuring optimum electrical conductivity while maintaining the mechanical properties of the OxPVA. More specifically, conductive OxPVA + MWCNT-S nanocomposite hydrogels displayed an interesting physicochemical profile, a typical macroscopic appearance and ultrastructure, a good mechanical behavior in the perspective of surgical implantation; additionally, *in vitro* cytotoxicity was excluded, and *in vivo* biocompatibility was verified. Considering that toxicity is likely dose and dispersion dependent [112], evidence was gathered that further support the functionalization adequacy.

According to study results, OxPVA + MWCNT-S are promising candidates for vanguard nerve conduits development; in the future, research works that consider the preclinical morpho-functional outcome associated with them in the presence of higher MWCNT-S concentrations in OxPVA will be fundamental to predict their possible future translation in clinical practice. Additionally, combining these new devices with electrical stimulation therapy could lead to a great improvement in nerve regeneration and nerve function following severe peripheral nerve injury. It appears that electrical stimulation may

enhance functional regeneration as a consequence of beneficial effects on myelin sheath thickness and axon diameter [113].

## Funding

This work was financially supported by the Department of Chemical Sciences of the University of Padua, project P-DISC#06BIRD2019-UNIPD.

Partially oxidized polyvinyl alcohol + functionalized water soluble multiwalled carbon nanotubes: a new conductive nanocomposite material with promising implications for neuroregeneration.

## CRediT authorship contribution statement

**Elena Stocco:** Conceptualization, Data curation, Formal analysis, Investigation, Methodology, Writing – original draft. **Silvia Barbon:** Data curation, Investigation, Writing – review & editing. **Ludovica Ceroni:** Data curation, Investigation, Writing – original draft. **Marta Confalonieri:** Data curation, Investigation, Writing – review & editing. **Giada Pulzato:** Investigation. **Samuel Pressi:** Data curation, Investigation. **Alice D'Ossualdo:** Data curation, Investigation. **Marta Contran:** Investigation. **Rafael Boscolo-Berto:** Investigation. **Cesare Tiengo:** Methodology. **Silvia Todros:** Data curation, Investigation, Methodology, Writing – review & editing. **Piero G. Pavan:** Methodology, Supervision, Writing – review & editing. **Veronica Macchi:** Methodology, Supervision, Writing – review & editing. **Raffaele De Caro:** Conceptualization, Supervision, Writing – review & editing. **Laura Calvillo:** Data curation, Methodology, Supervision. **Enzo Menna:** Conceptualization, Methodology, Supervision, Writing – review & editing. **Andrea Porzionato:** Conceptualization, Methodology, Supervision, Writing – review & editing.

## Declaration of competing interest

The authors declare that they have no known competing financial interests or personal relationships that could have appeared to influence the work reported in this paper.

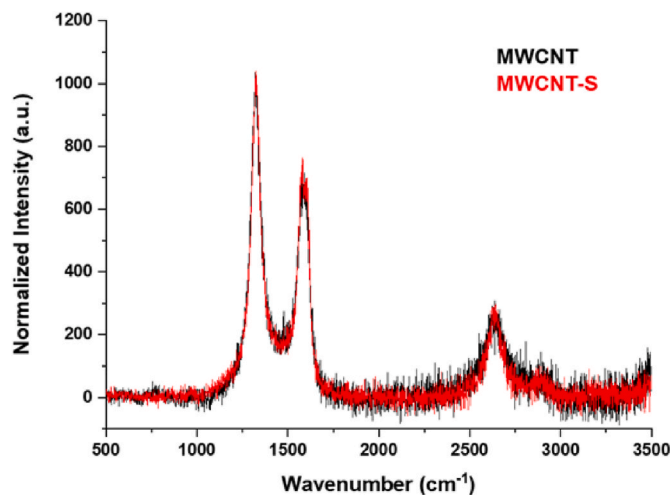


Figure A.1. Overlay of the Raman spectra of pristine MWCNT and MWCNT-S derivative; 633 nm excitation laser.

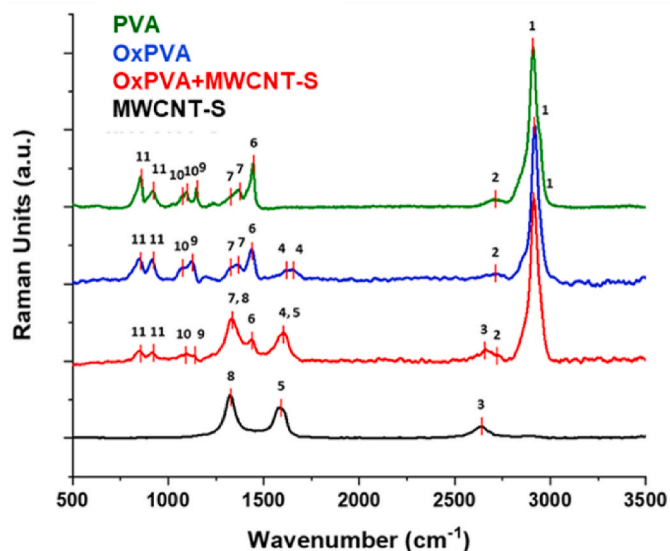


Figure A.2. Overlay of the IR spectra of pristine MWCNT and MWCNT-S derivative. Intensities were normalized, and Y axes values were shifted to better visualize peaks assignment (see Table A2 for peaks assignment).

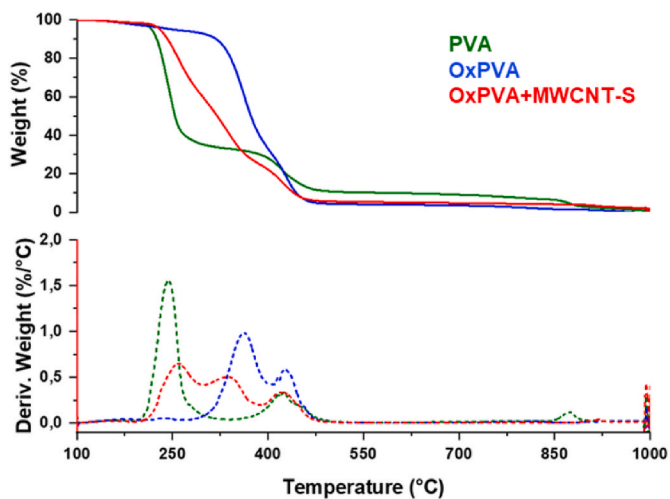


Figure A.3. Overlay of the thermograms (solid line) and the weight loss derivatives (dashed line) of PVA, OxPVA and OxPVA + MWCNT-S;  $10\text{ }^{\circ}\text{C min}^{-1}$  heating rate under nitrogen.

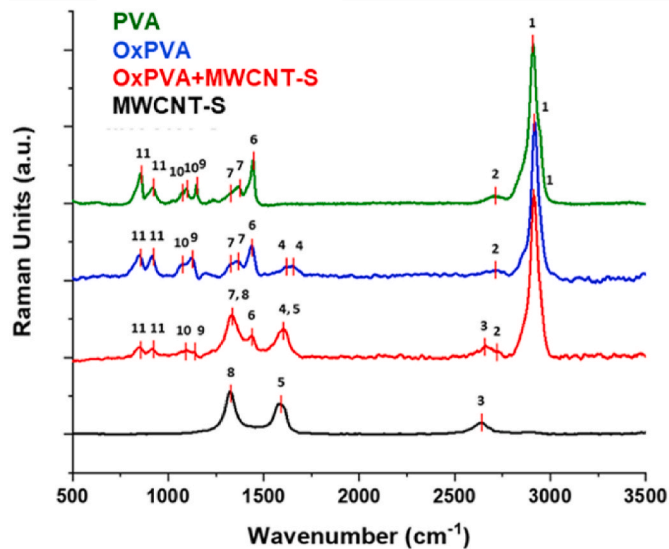


Figure A.5. Overlay of the Raman spectra of PVA, OxPVA, OxPVA + MWCNT-S and MWCNT-S. Intensities were normalized, and Y axes values were shifted to better visualize peaks assignment (see Table A2 for peaks assignment).

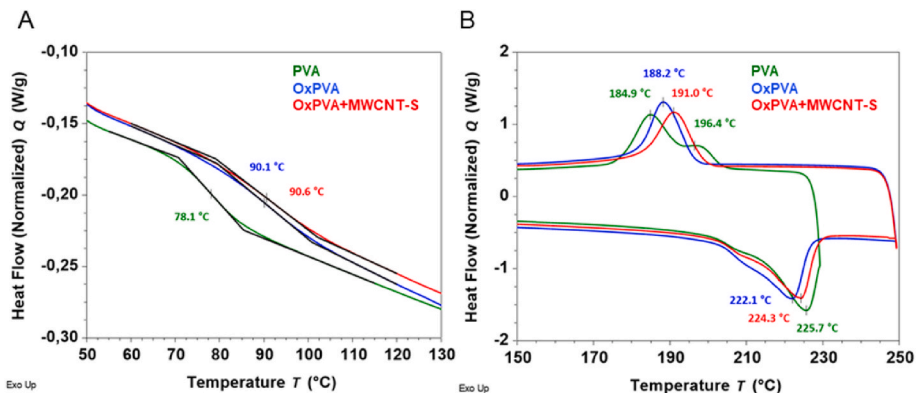


Figure A.4. Overlay of the DSC thermograms of PVA, OxPVA, OxPVA + MWCNT-S at  $10\text{ }^{\circ}\text{C min}^{-1}$ . A) Magnification of  $T_g$  relative to the first heating and cooling cycle, B) Magnification of  $T_m$  and  $T_c$  relative to the first heating and cooling cycle.

## Appendix A

### MWCNT-S IR spectroscopy

IR spectra were acquired between  $450\text{ cm}^{-1}$  and  $4000\text{ cm}^{-1}$  with a Nicolet Nexus 670 spectrometer at room temperature. The spectra were recorded with the KBr tablet technique with  $2\text{ cm}^{-1}$  resolution and accumulation of 20 scans. Spectra were processed using the software Origin 2018.

IR spectroscopy on pristine and functionalized nanotubes provides signals referable to MWCNTs in both samples (see Figure A2 and Table A2). In particular, at  $3434\text{ cm}^{-1}$  a broad signal of OH stretching could be attributed to the presence of oxygen groups, due to the partial oxidation that occurs during the purification process. Other weak peaks at  $2900\text{ cm}^{-1}$  were attributed to  $\text{CH}_x$  groups present in the sample maybe due to few structural defects [61,74]. The peak at  $1634\text{ cm}^{-1}$  could be attributed to the stretching of the carbon nanotube backbone and the peak at  $1565\text{ cm}^{-1}$  could be associated with the  $\text{C}=\text{C}$  bands of the aromatic ring. The peaks at lower wavenumbers were attributed to aromatic ring as well. Only few differences could be detected between pristine MWCNT and MWCNT-S derivative. In fact, the presence of functional groups in the product was very low compared to the carbon amount. The peak at  $3434\text{ cm}^{-1}$  was much more intense in the MWCNT-S sample probably due to the presence of bonded water which has increased affinity to the structure upon functionalization. The peak at  $1634\text{ cm}^{-1}$  appeared more intense in MWCNT-S possibly due to aromatic ring vibration of the sulphonated groups. The stretching vibrations of sulphonic groups  $\text{vs}(\text{SO}_3^-)$  were detected at  $1165\text{ cm}^{-1}$ , at  $1118\text{ cm}^{-1}$  and at  $1087\text{ cm}^{-1}$ , shifted at lower wavenumber compared to literature, allegedly due to the weakening of the bonds caused by electronic resonance with the nanotube structure [57].

**Table A.2**  
Assignment of signals from IR spectra of MWCNT and MWCNT-S (Figure A2).

N°	Assignment	Wavenumber ( $\text{cm}^{-1}$ )	
		MWCNT	MWCNT-S
1	O-H stretching	3434	3434
2	C-H aliphatic stretching	2913	2926–2859
3	O-H stretching from strong hydrogen-bond	2391	2394
4	–	2117	2115
5	$\text{C}=\text{C}$ stretching of the carbon nanotube backbone	1634	1630
6	$\text{C}=\text{C}$ stretching of the aromatic ring	1557	1436–1393
7	$\text{SO}_3^-$ stretching of the sulphonated group	–	1165–1087
8	Aromatic ring vibrations	1073–982	1039–1000
9	Aromatic ring vibrations	639	614

### Scaffolds Raman spectroscopy

Raman spectra of PVA, OxPVA and OxPVA + MWCNT-S are indicative of the different chemical compositions (Figure A5). PVA showed the characteristic stretching and bending signals of  $\text{CH}_2$  and  $\text{CH}-\text{OH}$  chemical groups between  $2911\text{ cm}^{-1}$  and  $1326\text{ cm}^{-1}$ , see details in Table A2 [76,77]. The signal at  $1147\text{ cm}^{-1}$  corresponds to the characteristic  $\text{C}-\text{O}$  band of the crystalline phase, the signal at  $1095\text{ cm}^{-1}$  referred to the other mode of  $\text{C}-\text{O}$  stretching and the peak at  $1072\text{ cm}^{-1}$  was attributed to the  $\text{C}-\text{OH}$  stretching [78]. Oxidized PVA showed the same spectrum as pure PVA except for the signal at  $1123\text{ cm}^{-1}$ , related to the asymmetric  $\text{C}-\text{OH}$  stretching characteristic of the amorphous domain of the material, instead of the signal at  $1147\text{ cm}^{-1}$  due to the crystalline phase in PVA [77,78]. This suggests a lower crystallinity of the polymer upon oxidation. In addition, new signals related to the formation of  $\text{C}=\text{C}$  and  $\text{C}=\text{O}$  double bonds, due to the oxidation process, were present. In particular, the peaks at  $1614\text{--}1652\text{ cm}^{-1}$  were attributed to stretching of isolated and conjugated  $\text{C}=\text{C}$  double bonds, and the signal at  $1652\text{ cm}^{-1}$  could also be attributed to  $\text{C}=\text{O}$  carbonyl groups [72]. The formation of double bonds could be a crucial factor in the breaking of hydrogen bonds between hydroxyl groups, leading to lower crystallinity in OxPVA [77]. MWCNT-S signals are clearly observed in OxPVA + MWCNT-S spectrum [28,79], partly overlapped to some of the OxPVA signals.

**Table A.2**  
Assignment of signals from Raman spectra of PVA, OxPVA, OxPVA + MWCNT-S and MWCNT-S (see Figure A5).

N°	Assignment	Wavenumber ( $\text{cm}^{-1}$ )			
		PVA	OxPVA	OxPVA + MWCNT-S	MWCNT-S
1	$\text{CH}_2$ stretching	2911	2917	2915	–
2	–	2717	2732	2730	–
3	CNT D* band	–	–	2658	2644
4	$\text{C}=\text{C}$ stretching single and conjugated	–	1652–1614	1600	–
5	$\text{C}=\text{O}$ stretching	–	–	1600	1591
6	CNT G band	–	–	1600	1591
7	$\text{CH}-\text{OH}$ bending	1443	1439	1440	–
8	$\text{CH}_2$ scissoring	–	–	–	–
9	$\text{CH}_2$ wagging	1371–1326	1369–1326	1332	–
10	$\text{CH}-\text{OH}$ bending	–	–	–	–
11	CNT D band	–	–	1332	1327
12	$\text{C}-\text{O}$ stretching	1147 (crystalline)	1123 (amorphous)	1140	–
13	$\text{C}-\text{O}$ stretching	1095–1072	1072	1096	–
14	$\text{C}-\text{OH}$ stretching	–	–	–	–
15	$\text{CH}_2$ rocking	918–855	916–850	916–851	–

## References

- [1] S. Shrestha, B.K. Shrestha, J. Lee, O.K. Joong, B.-S. Kim, C.H. Park, C.S. Kim, A conducting neural interface of polyurethane/silk-functionalized multiwall carbon nanotubes with enhanced mechanical strength for neuroregeneration, *Mater. Sci. Eng. C* 102 (2019) 511–523, <https://doi.org/10.1016/j.msec.2019.04.053>.
- [2] E. Stocco, S. Barbon, A. Emmi, C. Tiengo, V. Macchi, R. De Caro, A. Porzionato, Bridging gaps in peripheral nerves: from current strategies to future perspectives in conduit design, *Int. J. Mol. Sci.* 24 (2023) 9170, <https://doi.org/10.3390/ijms24119170>.
- [3] E. Stocco, S. Barbon, D. Faccio, L. Petrelli, D. Incendi, A. Zamuner, E. De Rose, M. Confalonieri, F. Tolomei, S. Todros, C. Tiengo, V. Macchi, M. Dettin, R. De Caro, A. Porzionato, Development and preclinical evaluation of bioactive nerve conduits for peripheral nerve regeneration: a comparative study, *Mater Today Bio* 22 (2023) 100761, <https://doi.org/10.1016/j.mtbio.2023.100761>.
- [4] M. Kasper, C. Deister, F. Beck, C.E. Schmidt, Bench-to-Bedside llearned: lommericalization of an acellular nerve graft, *Adv. Healthcare Mater.* 9 (2020), <https://doi.org/10.1002/adhm.202000174>.
- [5] N. Nicoli Aldini, M. Fini, M. Rocca, G. Giavaresi, R. Giardino, Guided regeneration with resorbable conduits in experimental peripheral nerve injuries, *Int. Orthop.* 24 (2000) 121–125, <https://doi.org/10.1007/s002640000142>.
- [6] M. Jahromi, S. Razavi, A. Bakhtiari, The advances in nerve tissue engineering: from fabrication of nerve conduit to *in vivo* nerve regeneration assays, *J Tissue Eng Regen Med* 13 (2019) 2077–2100, <https://doi.org/10.1002/term.2945>.
- [7] M. Rahman, T. Mahady Dip, R. Padhye, S. Houshyar, Review on electrically conductive smart nerve guide conduit for peripheral nerve regeneration, *J. Biomed. Mater. Res.* 111 (2023) 1916–1950, <https://doi.org/10.1002/jbm.a.37595>.
- [8] M. Anderson, N.B. Shelke, O.S. Manoukian, X. Yu, L.D. McCullough, S.G. Kumbar, Peripheral nerve regeneration strategies: electrically stimulating polymer based nerve growth conduits, *Crit. Rev. Biomed. Eng.* 43 (2015) 131–159, <https://doi.org/10.1615/CritRevBiomedEng.2015014015>.
- [9] F. Zhang, M. Zhang, S. Liu, C. Li, Z. Ding, T. Wan, P. Zhang, Application of hybrid electrically conductive hydrogels promotes peripheral nerve regeneration, *Gels* 8 (2022) 41, <https://doi.org/10.3390/gels8010041>.
- [10] P. Zarrintaj, E. Zangene, S. Manouchehri, L.M. Amirabad, N. Baheiraie, M. R. Hadjighasem, M. Farokhi, M.R. Ganjali, B.W. Walker, M.R. Saeb, M. Mozafari, S. Thomas, N. Annabi, Conductive biomaterials as nerve conduits: recent advances and future challenges, *Appl. Mater. Today* 20 (2020) 100784, <https://doi.org/10.1016/j.apmt.2020.100784>.
- [11] G. Kandhola, S. Park, J.-W. Lim, C. Chivers, Y.H. Song, J.H. Chung, J. Kim, J.-W. Kim, Nanomaterial-based scaffolds for tissue engineering applications: a review on graphene, carbon nanotubes and nanocellulose, *Tissue Eng Regen Med* 20 (2023) 411–433, <https://doi.org/10.1007/s13770-023-00530-3>.
- [12] V. Lovat, D. Pantarotto, L. Lagostena, B. Cacciari, M. Grandolfo, M. Righi, G. Spalluto, M. Prato, L. Ballerini, Carbon nanotube substrates boost neuronal electrical signaling, *Nano Lett.* 5 (2005) 1107–1110, <https://doi.org/10.1021/nl050637m>.
- [13] G. Cellot, E. Cilia, S. Cipollone, V. Rancic, A. Sucapane, S. Giordani, L. Gambazzi, H. Markram, M. Grandolfo, D. Scaini, F. Gelain, L. Casalis, M. Prato, M. Giugliano, L. Ballerini, Carbon nanotubes might improve neuronal performance by favouring electrical shortcuts, *Nat. Nanotechnol.* 4 (2009) 126–133, <https://doi.org/10.1038/nnano.2008.374>.
- [14] A. Kunisaki, A. Kodama, M. Ishikawa, T. Ueda, M.D. Lima, T. Kondo, N. Adachi, Carbon-nanotube yarns induce axonal regeneration in peripheral nerve defect, *Sci. Rep.* 11 (2021) 19562, <https://doi.org/10.1038/s41598-021-98603-7>.
- [15] C. Redondo-Gómez, R. Leandro-Mora, D. Blanch-Bermúdez, C. Espinoza-Araya, D. Hidalgo-Barrantes, J. Vega-Baudrit, Recent advances in carbon nanotubes for nervous tissue regeneration, *Adv. Polym. Technol.* 2020 (2020) 1–16, <https://doi.org/10.1155/2020/6861205>.
- [16] S. Marchesan, S. Bosi, A. Alshatwi, M. Prato, Carbon nanotubes for organ regeneration: an electrifying performance, *Nano Today* 11 (2016) 398–401, <https://doi.org/10.1016/j.nantod.2015.11.007>.
- [17] A. Fabbro, M. Prato, L. Ballerini, Carbon nanotubes in neuroregeneration and repair, *Adv. Drug Deliv. Rev.* 65 (2013) 2034–2044, <https://doi.org/10.1016/j.addr.2013.07.002>.
- [18] Z. Zhou, X. Liu, W. Wu, S. Park, A.L. Miller II, A. Terzic, L. Lu, Effective nerve cell modulation by electrical stimulation of carbon nanotube embedded conductive polymeric scaffolds, *Biomater. Sci.* 6 (2018) 2375–2385, <https://doi.org/10.1039/C8BM00553B>.
- [19] G. Scapin, P. Salice, S. Tescari, E. Menna, V. De Filippis, F. Filippini, Enhanced neuronal cell differentiation combining biomimetic peptides and a carbon nanotube-polymer scaffold, *Nanomedicine* 11 (2015) 621–632, <https://doi.org/10.1016/j.nano.2014.11.001>.
- [20] N. Vicentini, T. Gatti, P. Salice, G. Scapin, C. Marega, F. Filippini, E. Menna, Covalent functionalization enables good dispersion and anisotropic orientation of multi-walled carbon nanotubes in a poly(L-lactic acid) electrospun nanofibrous matrix boosting neuronal differentiation, *Carbon N Y* 95 (2015) 725–730, <https://doi.org/10.1016/j.carbon.2015.08.094>.
- [21] G. Scapin, T. Beralot, N. Vicentini, T. Gatti, S. Tescari, V. De Filippis, C. Marega, E. Menna, M. Gasparella, P.P. Parnigotto, R. Di Liddo, F. Filippini, Neuronal commitment of human circulating multipotent cells by carbon nanotube-polymer scaffolds and biomimetic peptides, *Nanomedicine* 11 (2016) 1929–1946, <https://doi.org/10.2217/nmm-2016-0150>.
- [22] M. Tonellato, M. Piccione, M. Gasparotto, P. Bellet, L. Tibauda, N. Vicentini, E. Bergantino, E. Menna, L. Vitiello, R. Di Liddo, F. Filippini, Commitment of autologous human multipotent stem cells on biomimetic poly-L-lactic acid-based scaffolds is strongly influenced by structure and concentration of carbon nanomaterial, *Nanomaterials* 10 (2020) 415, <https://doi.org/10.3390/nano10030415>.
- [23] T. Gatti, N. Vicentini, M. Mba, E. Menna, Organic functionalized carbon nanostructures for functional polymer-based nanocomposites, *Eur. J. Org. Chem.* 2016 (2016) 1071–1090, <https://doi.org/10.1002/ejoc.201501411>.
- [24] N. Vicentini, T. Gatti, M. Salerno, Y.S. Hernandez Gomez, M. Bellon, S. Gallio, C. Marega, F. Filippini, E. Menna, Effect of different functionalized carbon nanostructures as fillers on the physical properties of biocompatible poly(L-lactic acid) composites, *Mater. Chem. Phys.* 214 (2018) 265–276, <https://doi.org/10.1016/j.matchemphys.2018.04.042>.
- [25] Y. Liu, Y. Zhao, B. Sun, C. Chen, Understanding the toxicity of carbon nanotubes, *Acc. Chem. Res.* 46 (2013) 702–713, <https://doi.org/10.1021/ar300028m>.
- [26] P. Salice, E. Fabris, C. Sartorio, D. Fenaroli, V. Figà, M.P. Casaletto, S. Cataldo, B. Pignataro, E. Menna, An insight into the functionalisation of carbon nanotubes by diazonium chemistry: towards a controlled decoration, *Carbon N Y* 74 (2014) 73–82, <https://doi.org/10.1016/j.carbon.2014.02.084>.
- [27] O. Koysuren, Preparation and characterization of polyvinyl alcohol/carbon nanotube (PVA/CNT) conductive nanofibers, *J. Polym. Eng.* 32 (2012) 407–413, <https://doi.org/10.1515/poleng-2012-0068>.
- [28] F.-P. Du, E.-Z. Ye, W. Yang, T.-H. Shen, C.-Y. Tang, X.-L. Xie, X.-P. Zhou, W.-C. Law, Electroactive shape memory polymer based on optimized multi-walled carbon nanotubes/polyvinyl alcohol nanocomposites, *Compos. B Eng.* 68 (2015) 170–175, <https://doi.org/10.1016/j.compositesb.2014.08.043>.
- [29] A. Chebil, B. Ben Doudou, C. Dridi, M. Dammak, Synthesis characterization, optical and electrical properties of polyvinyl alcohol/multi-walled carbon nanotube nanocomposites: a composition dependence study, *Mater. Sci. Eng., B* 243 (2019) 125–130, <https://doi.org/10.1016/j.mseb.2019.04.004>.
- [30] M. Nabipour, A. Mellati, M. Abasi, S.E. Barough, A. Karimizade, P. Banikarimi, E. Hasanazadeh, Preparation of bilayer tissue-engineered polyurethane/poly-L-lactic acid nerve conduits and their *in vitro* characterization for use in peripheral nerve regeneration, *J. Biol. Eng.* 18 (2024) 16, <https://doi.org/10.1186/s13036-024-00412-9>.
- [31] B. Anis, W.K.B. Khalil, N.A. Kamel, S.L. Abd El-Messieh, Preparation, characterization, and genotoxicity of Polyvinyl alcohol-single-wall carbon nanotubes (PVA/SWCNTs) nanocomposites for tissue engineering applications, *Adv. Nat. Sci. Nanosci. Nanotechnol.* 12 (2021) 045017, <https://doi.org/10.1088/2043-6262/ac4aeb>.
- [32] X. Liu, J.C. Kim, A.L. Miller, B.E. Waletzki, L. Lu, Electrically conductive nanocomposite hydrogels embedded with functionalized carbon nanotubes for spinal cord injury, *New J. Chem.* 42 (2018) 17671–17681, <https://doi.org/10.1039/C8NJ03038C>.
- [33] A.R. Nectow, K.G. Marra, D.L. Kaplan, Biomaterials for the development of peripheral nerve guidance conduits, *Tissue Eng., Part B* 18 (2012) 40–50, <https://doi.org/10.1089/ten.teb.2011.0240>.
- [34] A. Porzionato, S. Barbon, E. Stocco, D. Dalzoppo, M. Contran, E. De Rose, P. P. Parnigotto, V. Macchi, C. Grandi, R. De Caro, Development of oxidized polyvinyl alcohol-based nerve conduits coupled with the ciliary neurotrophic factor, *Materials* 12 (2019) 1996, <https://doi.org/10.3390/ma12121996>.
- [35] E. Stocco, S. Barbon, F. Grandi, P.G. Gamba, L. Boggio, C. Del Gaudio, D. Dalzoppo, S. Lora, S. Rajendran, A. Porzionato, V. Macchi, A. Rambaldo, R. De Caro, P.P. Parnigotto, C. Grandi, Partially oxidized polyvinyl alcohol as a promising material for tissue engineering, *J Tissue Eng Regen Med* 11 (2017) 2060–2070, <https://doi.org/10.1002/term.2101>.
- [36] E. Stocco, S. Barbon, L. Lora, F. Grandi, L. Sartore, C. Tiengo, L. Petrelli, D. Dalzoppo, P.P. Parnigotto, V. Macchi, R. De Caro, A. Porzionato, C. Grandi, Partially oxidized polyvinyl alcohol conduit for peripheral nerve regeneration, *Sci. Rep.* 8 (2018) 604, <https://doi.org/10.1038/s41598-017-19058-3>.
- [37] E. Stocco, S. Barbon, V. Macchi, C. Tiengo, L. Petrelli, A. Rambaldo, A. Borean, S. Capelli, A. Filippi, F. Romanato, P.P. Parnigotto, C. Grandi, R. De Caro, A. Porzionato, New bioresorbable wraps based on oxidized polyvinyl alcohol and leukocyte-fibrin-platelet membrane to support peripheral nerve neurotrophin: preclinical comparison versus NeuraWrap, *Sci. Rep.* 9 (2019) 17193, <https://doi.org/10.1038/s41598-019-53812-z>.
- [38] E. Stocco, S. Barbon, A. Lamanna, E. De Rose, A. Zamuner, D. Sandrin, M. Marsotto, A. Auditore, G.M.L. Messina, A. Licciardello, G. Iucci, V. Macchi, R. De Caro, M. Dettin, A. Porzionato, Bioactivated oxidized polyvinyl alcohol towards next-generation nerve conduits development, *Polymers* 13 (2021) 3372, <https://doi.org/10.3390/polym13193372>.
- [39] J. Park, J. Jeon, B. Kim, M.S. Lee, S. Park, J. Lim, J. Yi, H. Lee, H.S. Yang, J.Y. Lee, Electrically conductive hydrogel nerve guidance conduits for peripheral nerve regeneration, *Adv. Funct. Mater.* 30 (2020), <https://doi.org/10.1002/adfm.202003759>.
- [40] J.M. Vensi Basso, I. Yurchenko, M. Simon, D.J. Rizzo, C. Staii, Role of geometrical cues in neuronal growth, *Phys. Rev. E* 99 (2019) 022408, <https://doi.org/10.1103/PhysRevE.99.022408>.
- [41] W. Xue, W. Shi, Y. Kong, M. Kuss, B. Duan, Anisotropic scaffolds for peripheral nerve and spinal cord regeneration, *Bioact. Mater.* 6 (2021) 4141–4160, <https://doi.org/10.1016/j.bioactmat.2021.04.019>.
- [42] S. Barbon, E. Stocco, M. Contran, F. Facchin, R. Boscolo-Berto, S. Todros, D. Sandrin, F. Romanato, P. Pavan, V. Macchi, V. Vindigni, F. Bassetto, R. De Caro, A. Porzionato, Preclinical development of bioengineered allografts derived



- from decellularized human diaphragm, *Biomedicine* 10 (2022) 739, <https://doi.org/10.3390/biomedicine10040739>.
- [43] C.J. Thiele, Neuroblastoma cell lines, in: *Human Cell Culture*, J. Human Cell Culture vol. 1, 1998, pp. 21–53.
- [44] D. Arslantunali, G. Budak, V. Hasirci, Multiwalled CNT-PHEMA composite conduit for peripheral nerve repair, *J. Biomed. Mater. Res.* 102 (2014) 828–841, <https://doi.org/10.1002/jbm.a.34727>.
- [45] M.-H. Yang, K.-C. Chen, P.-W. Chiang, T.-W. Chung, W.-J. Chen, P.-Y. Chu, S.-C.-J. Chen, Y.-S. Lu, C.-H. Yuan, M.-C. Wang, C.-Y. Lin, Y.-F. Huang, S.-B. Jong, P.-C. Lin, Y.-C. Tyan, Proteomic profiling of neuroblastoma cells adhesion on hyaluronic acid-based surface for neural tissue engineering, *BioMed Res. Int.* (2016) 1–13, <https://doi.org/10.1155/2016/1917394>, 2016.
- [46] J.L. Bahr, J. Yang, D.V. Kosynkin, M.J. Bronikowski, R.E. Smalley, J.M. Tour, Functionalization of carbon nanotubes by electrochemical reduction of aryl diazonium salts: a bucky paper electrode, *J. Am. Chem. Soc.* 123 (2001) 6536–6542, <https://doi.org/10.1021/ja010462s>.
- [47] L. Ghasemi-Mobarakeh, M.P. Prabhakaran, M. Morshed, M.H. Nasr-Esfahani, H. Baharvand, S. Kiani, S.S. Al-Deyab, S. Ramakrishna, Application of conductive polymers, scaffolds and electrical stimulation for nerve tissue engineering, *J. Tissue Eng Regen Med* 5 (2011) e17–e35, <https://doi.org/10.1002/term.383>.
- [48] H. Xuan, S. Wu, Y. Jin, S. Wei, F. Xiong, Y. Xue, B. Li, Y. Yang, H. Yuan, A bioinspired self-healing conductive hydrogel promoting peripheral nerve regeneration, *Adv. Sci.* 10 (2023), <https://doi.org/10.1002/adv.202302519>.
- [49] E.N. Zare, P. Makvandi, B. Ashtari, F. Rossi, A. Motahari, G. Perale, Progress in conductive polyaniline-based nanocomposites for biomedical applications: a review, *J. Med. Chem.* 63 (2020) 1–22, <https://doi.org/10.1021/acs.jmedchem.9b00803>.
- [50] H. Xu, J.M. Holzwarth, Y. Yan, P. Xu, H. Zheng, Y. Yin, S. Li, P.X. Ma, Conductive PPY/PDLLA conduit for peripheral nerve regeneration, *Biomaterials* 35 (2014) 225–235, <https://doi.org/10.1016/j.biomaterials.2013.10.002>.
- [51] S. Cui, J. Mao, M. Rouabhi, S. Elkoun, Z. Zhang, A biocompatible polypyrrole membrane for biomedical applications, *RSC Adv.* 11 (2021) 16996–17006, <https://doi.org/10.1039/D1RA01338F>.
- [52] L. Huang, X. Yang, L. Deng, D. Ying, A. Lu, L. Zhang, A. Yu, B. Duan, Biocompatible chitin hydrogel incorporated with PEDOT nanoparticles for peripheral nerve repair, *ACS Appl. Mater. Interfaces* 13 (2021) 16106–16117, <https://doi.org/10.1021/acsami.1c01904>.
- [53] H. Yi, R. Patel, K.D. Patel, L.-S. Bouchard, A. Jha, A.W. Perriman, M. Patel, Conducting polymer-based scaffolds for neuronal tissue engineering, *J. Mater. Chem. B* 11 (2023) 11006–11023, <https://doi.org/10.1039/D3TB01838E>.
- [54] A.A. Adewunmi, S. Ismail, A.S. Sultan, Carbon nanotubes (CNTs) nanocomposite hydrogels developed for various applications: a critical review, *J. Inorg. Organomet. Polym. Mater.* 26 (2016) 717–737, <https://doi.org/10.1007/s10904-016-0379-6>.
- [55] J. Liu, T. Zou, Y. Zhang, J. Koh, H. Li, Y. Wang, Y. Zhao, C. Zhang, Three-dimensional electroconductive carbon nanotube-based hydrogel scaffolds enhance neural differentiation of stem cells from apical papilla, *Biomater. Adv.* 138 (2022) 212868, <https://doi.org/10.1016/j.bioadv.2022.212868>.
- [56] Y. Liu, Y. Shen, L. Sun, J. Li, C. Liu, W. Ren, F. Li, L. Gao, J. Chen, F. Liu, Y. Sun, N. Tang, H.-M. Cheng, Y. Du, Elemental superdoping of graphene and carbon nanotubes, *Nat. Commun.* 7 (2016) 10921, <https://doi.org/10.1038/ncomms10921>.
- [57] P. Salice, C. Sartorio, A. Burlini, R. Improta, B. Pignataro, E. Menna, On the trade-off between processability and opto-electronic properties of single wall carbon nanotube derivatives in thin film heterojunctions, *J. Mater. Chem. C* 3 (2015) 303–312, <https://doi.org/10.1039/C4TC01350F>.
- [58] M.R. Heinrich, Intermolecular orbital functionalisation involving aryl radicals generated from arenediazonium salts, *Chem. Eur. J.* 15 (2009) 820–833, <https://doi.org/10.1002/chem.200801306>.
- [59] M. Schirowski, F. Hauke, A. Hirsch, Controlling the degree of functionalization: in-depth quantification and side-product analysis of diazonium chemistry on SWCNTs, *Chem. Eur. J.* 25 (2019) 12761–12768, <https://doi.org/10.1002/chem.201902330>.
- [60] S. Fleutot, J.-C. Dupin, G. Renaudin, H. Martinez, Intercalation and grafting of benzene derivatives into zinc–aluminum and copper–chromium layered double hydroxide hosts: an XPS monitoring study, *Phys. Chem. Chem. Phys.* 13 (2011) 17564, <https://doi.org/10.1039/c1cp20453j>.
- [61] S. Fleutot, H. Martinez, J.C. Dupin, I. Baraille, C. Forano, G. Renaudin, D. Gonbeau, Experimental (X-Ray Photoelectron Spectroscopy) and theoretical studies of benzene based organics intercalated into layered double hydroxide, *Solid State Sci.* 13 (2011) 1676–1686, <https://doi.org/10.1016/j.solidstatesciences.2011.05.007>.
- [62] M. D'Este, M. De Nardi, E. Menna, A Co-functionalization approach to soluble and functional single-walled carbon nanotubes, *Eur. J. Org. Chem.* 2006 (2006) 2517–2522, <https://doi.org/10.1002/ejoc.200600196>.
- [63] S. Bhattacharjee, DLS and zeta potential – what they are and what they are not? *J. Contr. Release* 235 (2016) 337–351, <https://doi.org/10.1016/j.jconrel.2016.06.017>.
- [64] L. Reinert, M. Zeiger, S. Suárez, V. Presser, F. Mücklich, Dispersion analysis of carbon nanotubes, carbon onions, and nanodiamonds for their application as reinforcement phase in nickel metal matrix composites, *RSC Adv.* 5 (2015) 95149–95159, <https://doi.org/10.1039/CSRA14310A>.
- [65] R. Li, X. Wang, Z. Ji, B. Sun, H. Zhang, C.H. Chang, S. Lin, H. Meng, Y.-P. Liao, M. Wang, Z. Li, A.A. Hwang, T.-B. Song, R. Xu, Y. Yang, J.I. Zink, A.E. Nel, T. Xia, Surface charge and cellular processing of covalently functionalized multiwall carbon nanotubes determine pulmonary toxicity, *ACS Nano* 7 (2013) 2352–2368, <https://doi.org/10.1021/nn305567s>.
- [66] A. Abdulhameed, M.N. Mohtar, M.N. Hamidon, I.A. Halin, Mild nitric acid treatments to improve multi-walled carbon nanotubes dispersity and solubility in dielectrophoresis mediums, *Fullerenes, Nanotubes and, Carbon Nanostructures* 29 (2021) 832–839, <https://doi.org/10.1080/1536383X.2021.1908999>.
- [67] B. White, S. Banerjee, S. O'Brien, N.J. Turro, I.P. Herman, Zeta-potential measurements of surfactant-wrapped individual single-walled carbon nanotubes, *J. Phys. Chem. C* 111 (2007) 13684–13690, <https://doi.org/10.1021/jp070853e>.
- [68] B. Salopek, D. Krasi, S. Filipovi, Measurement and Application of Zeta-Potential, *Rudarsko-Geološko-Naftni Zbornik*, 2023.
- [69] Z. Yang, D. Xu, J. Liu, J. Liu, L. Li, L. Zhang, J. Lv, Fabrication and characterization of poly(vinyl alcohol)/carbon nanotube melt-spinning composites fiber, *Prog. Nat. Sci.: Mater. Int.* 25 (2015) 437–444, <https://doi.org/10.1016/j.pnsc.2015.09.014>.
- [70] K.S. Hajeessa, M.A. Hussein, Y. Anwar, N.Y. Tashkandi, Z.M. Al-amshany, Nanocomposites containing polyvinyl alcohol and reinforced carbon-based nanofiller, *Nanobiomedicine (Rij)* 5 (2018) 184954351879481, <https://doi.org/10.1177/1849543518794818>.
- [71] M.J. Yee, N.M. Mubarak, M. Khalid, E.C. Abdullah, P. Jagadish, Synthesis of polyvinyl alcohol (PVA) infiltrated MWCNTs buckypaper for strain sensing application, *Sci. Rep.* 8 (2018) 17295, <https://doi.org/10.1038/s41598-018-35638-3>.
- [72] B. Gupta, S. Anjum, S. Ikram, Characterization and physicochemical studies of crosslinked thiolated polyvinyl alcohol hydrogels, *Polym. Bull.* 70 (2013) 2709–2725, <https://doi.org/10.1007/s00289-013-0982-4>.
- [73] J. Ribeiro, A.R. Caseiro, T. Pereira, A.A. Armada-da-Silva, I. Pires, J. Prada, I. Amorim, I. Leal Reis, S. Amado, J.D. Santos, S. Bompasso, S. Raimondo, A.S. P. Varejão, S. Geuna, A.L. Luís, A.C. Maurício, Evaluation of PVA biodegradable electric conductive membranes for nerve regeneration in axonotmesis injuries: the rat sciatic nerve animal model, *J. Biomed. Mater. Res.* 105 (2017) 1267–1280, <https://doi.org/10.1002/jbm.a.35998>.
- [74] N. Jamil, H. Husin, A.W. Alfida, Z. Aman, Z. Hassan, Characterization and preparation of polyvinyl alcohol (PVA) as inhibitor in formation of hydrates, *International Journal of Current Research in Science, Engineering & Technology* 1 (2018) 578, <https://doi.org/10.30967/ijcrset.1.S1.2018.578-584>.
- [75] P.A. Putro, A.S. Sulaeman, A. Maddu, Polyvinyl alcohol-based hydrogel: a systematic literature review on thermal properties by differential scanning Calorimetry, *J. Phys. Conf. Ser.* 2019 (2021) 012101, <https://doi.org/10.1088/1742-6596/2019/1/012101>.
- [76] M. Hidalgo, H. Reinecke, C. Mijangos, PVC containing hydroxyl groups, *Polymer* 40 (1999) 3535–3543, [https://doi.org/10.1016/S0032-3861\(98\)00568-0](https://doi.org/10.1016/S0032-3861(98)00568-0).
- [77] B.J. Holland, J.N. Hay, The thermal degradation of poly(vinyl alcohol), *Polymer* 42 (2001) 6775–6783, [https://doi.org/10.1016/S0032-3861\(01\)00166-5](https://doi.org/10.1016/S0032-3861(01)00166-5).
- [78] O. Probst, E.M. Moore, D.E. Resasco, B.P. Grady, Nucleation of polyvinyl alcohol crystallization by single-walled carbon nanotubes, *Polymer* 45 (2004) 4437–4443, <https://doi.org/10.1016/j.polymer.2004.04.031>.
- [79] Y. Bin, M. Mine, A. Koganemaru, X. Jiang, M. Matsuo, Morphology and mechanical and electrical properties of oriented PVA-VGCF and PVA-MWNT composites, *Polymer* 47 (2006) 1308–1317, <https://doi.org/10.1016/j.polymer.2005.12.032>.
- [80] M. Ekrem, Mechanical properties of MWCNT reinforced polyvinyl alcohol nanofiber mats by electrospinning method, *El-Cezeri Fen ve Mühendislik Dergisi* 4 (2017) 190–200, <https://doi.org/10.31202/ecjse.305851>.
- [81] C. Li, J. Vongsvivut, X. She, Y. Li, F. She, L. Kong, New insight into non-isothermal crystallization of PVA–graphene composites, *Phys. Chem. Chem. Phys.* 16 (2014) 22145–22158, <https://doi.org/10.1039/C4CP03613A>.
- [82] D. Thomas, P. Cebe, Self-nucleation and crystallization of polyvinyl alcohol, *J. Therm. Anal. Calorim.* 127 (2017) 885–894, <https://doi.org/10.1007/s10973-016-5811-1>.
- [83] C. Li, T. Hou, J. Vongsvivut, Y. Li, X. She, F. She, W. Gao, L. Kong, Simultaneous crystallization and decomposition of PVA/MMT composites during non-isothermal process, *Thermochim. Acta* 618 (2015) 26–35, <https://doi.org/10.1016/j.tca.2015.09.009>.
- [84] Y. Zhu, C. Wu, Y. Zhang, J. Zhao, Study on the chain entanglement of polyvinyl alcohol fiber during the dry-jet wet spinning process, *Fibers Polym.* 16 (2015) 345–353, <https://doi.org/10.1007/s12221-015-0345-x>.
- [85] S. Barbon, E. Stocco, D. Dalzoppo, S. Todros, A. Canale, R. Boscolo-Berto, P. Pavan, V. Macchi, C. Grandi, R. De Caro, A. Porzionato, Halogen-mediated partial oxidation of polyvinyl alcohol for tissue engineering purposes, *Int. J. Mol. Sci.* 21 (2020) 801, <https://doi.org/10.3390/ijms21030801>.
- [86] J.-C. Jhang, J.-H. Lin, C.-W. Lou, Y.-S. Chen, Biodegradable and conductive PVA/CNT nanofibrous membranes used in nerve conduit applications, *J. Ind. Textil.* 51 (2022) 10485–10655, <https://doi.org/10.1177/15280837211032086>.
- [87] A. Markov, R. Wördenweber, L. Ichkitidze, A. Gerasimenko, U. Kurilova, I. Suetina, M. Mezentseva, A. Offenhäuser, D. Telyshev, Biocompatible SWCNT conductive composites for biomedical applications, *Nanomaterials* 10 (2020) 2492, <https://doi.org/10.3390/nano10122492>.
- [88] W. Zhao, H. Tu, J. Chen, J. Wang, H. Liu, F. Zhang, J. Li, Functionalized hydrogels in neural injury repairing, *Front. Neurosci.* 17 (2023), <https://doi.org/10.3389/fnins.2023.1199299>.
- [89] M. Mihajlovic, M. Mihajlovic, P.Y.W. Dankers, R. Masereeuw, R.P. Sijbesma, Carbon nanotube reinforced supramolecular hydrogels for bioapplications, *Macromol. Biosci.* 19 (2019) 1800173, <https://doi.org/10.1002/mabi.201800173>.

- [90] M. Salehi, M. Naseri-Nosar, S. Ebrahimi-Barough, M. Nourani, A. Khojasteh, A.-A. Hamidieh, A. Amani, S. Farzamfar, J. Ai, Sciatic nerve regeneration by transplantation of Schwann cells via erythropoietin controlled-releasing polylactic acid/multiwalled carbon nanotubes/gelatin nanofibrils neural guidance conduit, *J. Biomed. Mater. Res. B Appl. Biomater.* 106 (2018) 1463–1476, <https://doi.org/10.1002/jbm.b.33952>.
- [91] H. Ravanbakhsh, G. Bao, N. Latifi, L.G. Mongeau, Carbon nanotube composite hydrogels for vocal fold tissue engineering: biocompatibility, rheology, and porosity, *Mater. Sci. Eng. C* 103 (2019) 109861, <https://doi.org/10.1016/j.msec.2019.109861>.
- [92] L. Suo, H. Wu, P. Wang, Z. Xue, J. Gao, J. Shen, The improvement of periodontal tissue regeneration using a <sc>3D</sc>-printed carbon nanotube/chitosan/sodium alginate composite scaffold, *J. Biomed. Mater. Res. B Appl. Biomater.* 111 (2023) 73–84, <https://doi.org/10.1002/jbm.b.35133>.
- [93] W. Lan, X. Zhang, M. Xu, L. Zhao, D. Huang, X. Wei, W. Chen, Carbon nanotube reinforced polyvinyl alcohol/biphasic calcium phosphate scaffold for bone tissue engineering, *RSC Adv.* 9 (2019) 38998–39010, <https://doi.org/10.1039/C9RA08569F>.
- [94] A.T. Gubaidullin, A.O. Makarova, S.R. Derkach, N.G. Voron'ko, A.I. Kadyrov, S. A. Ziganshina, V.V. Salnikov, O.S. Zueva, Y.F. Zuev, Modulation of molecular structure and mechanical properties of  $\kappa$ -carrageenan-gelatin hydrogel with multi-walled carbon nanotubes, *Polymers* 14 (2022) 2346, <https://doi.org/10.3390/polym14122346>.
- [95] B.S. Boyd, C. Puttlitz, J. Gan, K.S. Topp, Strain and excursion in the rat sciatic nerve during a modified straight leg raise are altered after traumatic nerve injury, *J. Orthop. Res.* 23 (2005) 764–770, <https://doi.org/10.1016/j.orthres.2004.11.008>.
- [96] S.R. Shin, H. Bae, J.M. Cha, J.Y. Mun, Y.-C. Chen, H. Tekin, H. Shin, S. Zarabi, M. R. Dokmeci, S. Tang, A. Khademhosseini, Carbon nanotube reinforced hybrid microgels as scaffold materials for cell encapsulation, *ACS Nano* 6 (2012) 362–372, <https://doi.org/10.1021/nn203711s>.
- [97] S. Ahadian, J. Ramón-Azcón, M. Estili, X. Liang, S. Ostrovidov, H. Shiku, M. Ramalingam, K. Nakajima, Y. Sakka, H. Bae, T. Matsue, A. Khademhosseini, Hybrid hydrogels containing vertically aligned carbon nanotubes with anisotropic electrical conductivity for muscle myofiber fabrication, *Sci. Rep.* 4 (2014) 4271, <https://doi.org/10.1038/srep04271>.
- [98] M.-H. Alves, B.E.B. Jensen, A.A.A. Smith, A.N. Zelikin, Poly(Vinyl alcohol) physical hydrogels: new vista on a long serving biomaterial, *Macromol. Biosci.* 11 (2011) 1293–1313, <https://doi.org/10.1002/mabi.201100145>.
- [99] M.I. Baker, S.P. Walsh, Z. Schwartz, B.D. Boyan, A review of polyvinyl alcohol and its uses in cartilage and orthopedic applications, *J. Biomed. Mater. Res. B Appl. Biomater.* 100B (2012) 1451–1457, <https://doi.org/10.1002/jbm.b.32694>.
- [100] E. Stocco, S. Barbon, D. Dalzoppo, S. Lora, L. Sartore, M. Folin, P.P. Parnigotto, C. Grandi, Tailored PVA/ECM scaffolds for cartilage regeneration, *BioMed Res. Int.* 2014 (2014) 1–12, <https://doi.org/10.1155/2014/762189>.
- [101] E. Stocco, S. Barbon, P. Radossi, S. Rajendran, D. Dalzoppo, M. Bortolami, A. Bagno, F. Grandi, P.G. Gamba, P.P. Parnigotto, G. Tagariello, C. Grandi, Autologous chondrocytes as a novel source for neo-chondrogenesis in haemophiliacs, *Cell Tissue Res.* 366 (2016) 51–61, <https://doi.org/10.1007/s00441-016-2408-8>.
- [102] F. Grandi, E. Stocco, S. Barbon, A. Rambaldo, M. Contran, F. Fascetti Leon, P. Gamba, P.P. Parnigotto, V. Macchi, R. De Caro, A. Porzionato, Composite scaffolds based on intestinal extracellular matrices and oxidized polyvinyl alcohol: a preliminary study for a new regenerative approach in short bowel syndrome, *BioMed Res. Int.* 2018 (2018) 1–13, <https://doi.org/10.1155/2018/7824757>.
- [103] M.A. Saleemi, M. Hosseini Fouladi, P.V.C. Yong, K. Chinna, N.K. Palanisamy, E. H. Wong, Toxicity of carbon nanotubes: molecular mechanisms, signaling cascades, and remedies in biomedical applications, *Chem. Res. Toxicol.* 34 (2021) 24–46, <https://doi.org/10.1021/acs.chemrestox.0c00172>.
- [104] M.C. Serrano, M.C. Gutiérrez, F. del Monte, Role of polymers in the design of 3D carbon nanotube-based scaffolds for biomedical applications, *Prog. Polym. Sci.* 39 (2014) 1448–1471, <https://doi.org/10.1016/j.progpolymsci.2014.02.004>.
- [105] K. Shah, D. Vasileva, A. Karadaghy, S.P. Zusiak, Development and characterization of polyethylene glycol–carbon nanotube hydrogel composite, *J. Mater. Chem. B* 3 (2015) 7950–7962, <https://doi.org/10.1039/C5TB01047K>.
- [106] S. Sharma, S. Naskar, K. Kuotsu, A review on carbon nanotubes: influencing toxicity and emerging carrier for platinum based cytotoxic drug application, *J. Drug Deliv. Sci. Technol.* 51 (2019) 708–720, <https://doi.org/10.1016/j.jddst.2019.02.028>.
- [107] H.-C. Ni, T.-C. Tseng, J.-R. Chen, S. Hsu, I.-M. Chiu, Fabrication of bioactive conduits containing the fibroblast growth factor 1 and neural stem cells for peripheral nerve regeneration across a 15 mm critical gap, *Biofabrication* 5 (2013) 035010, <https://doi.org/10.1088/1758-5082/5/3/035010>.
- [108] I.H. Yang, C.C. Co, C.-C. Ho, Controlling neurite outgrowth with patterned substrates, *J. Biomed. Mater. Res.* 97A (2011) 451–456, <https://doi.org/10.1002/jbm.a.33082>.
- [109] M. Sun, M. McGowan, P.J. Kingham, G. Terenghi, S. Downes, Novel thin-walled nerve conduit with microgrooved surface patterns for enhanced peripheral nerve repair, *J. Mater. Sci. Mater. Med.* 21 (2010) 2765–2774, <https://doi.org/10.1007/s10856-010-4120-7>.
- [110] L. Yao, S. Wang, W. Cui, R. Sherlock, C. O'Connell, G. Damodaran, A. Gorman, A. Windebank, A. Pandit, Effect of functionalized micropatterned PLGA on guided neurite growth, *Acta Biomater.* 5 (2009) 580–588, <https://doi.org/10.1016/j.actbio.2008.09.002>.
- [111] MaC. Acosta-García, I. Morales-Reyes, A. Jiménez-Anguiano, N. Batina, N. P. Castellanos, R. Godínez-Fernández, Simultaneous recording of electrical activity and the underlying ionic currents in NG108-15 cells cultured on gold substrate, *Heliyon* 4 (2018) e00550, <https://doi.org/10.1016/j.heliyon.2018.e00550>.
- [112] L. Zhou, H.J. Forman, Y. Ge, J. Lunec, Multi-walled carbon nanotubes: a cytotoxicity study in relation to functionalization, dose and dispersion, *Toxicol. Vitro* 42 (2017) 292–298, <https://doi.org/10.1016/j.tiv.2017.04.027>.
- [113] S. Hasiba-Pappas, L.-P. Kamolz, H. Luze, S.P. Nischwitz, J.C.J. Holzer-Geissler, A. C. Tuca, T. Rienmüller, M. Polz, D. Ziesel, R. Winter, Does electrical stimulation through nerve conduits improve peripheral nerve regeneration?—a systematic review, *J. Personalized Med.* 13 (2023) 414, <https://doi.org/10.3390/jpm13030414>.